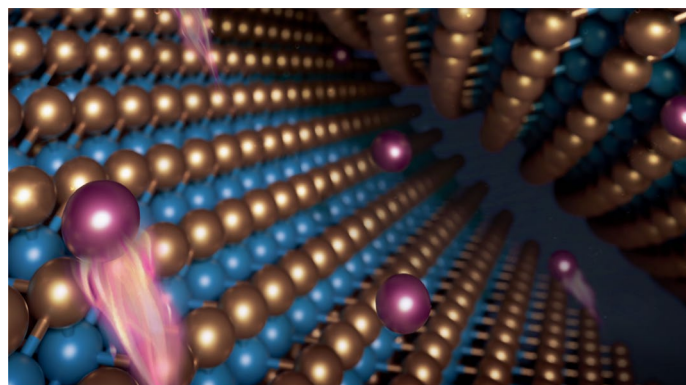


Intercalation in 2D materials and in situ studies

Ruijie Yang ^{1,2,11}, Liang Mei ^{1,11}, Zhaoyang Lin ^{3,11}, Yingying Fan², Jongwoo Lim ⁴, Jinghua Guo ⁵, Yijin Liu ⁶, Hyeon Suk Shin ⁷, Damien Voiry ⁸, Qingye Lu ²✉, Ju Li ⁹✉ & Zhiyuan Zeng ^{1,10}✉

Abstract

Intercalation of atoms, ions and molecules is a powerful tool for altering or tuning the properties – interlayer interactions, in-plane bonding configurations, Fermi-level energies, electronic band structures and spin–orbit coupling – of 2D materials. Intercalation can induce property changes in materials related to photonics, electronics, optoelectronics, thermoelectricity, magnetism, catalysis and energy storage, unlocking or improving the potential of 2D materials in present and future applications. In situ imaging and spectroscopy technologies are used to visualize and trace intercalation processes. These techniques provide the opportunity for deciphering important and often elusive intercalation dynamics, chemomechanics and mechanisms, such as the intercalation pathways, reversibility, uniformity and speed. In this Review, we discuss intercalation in 2D materials, beginning with a brief introduction of the intercalation strategies, then we look into the atomic and intrinsic effects of intercalation, followed by an overview of their in situ studies, and finally provide our outlook.



A full list of affiliations appears at the end of the paper. ✉ e-mail: qingye.lu@ucalgary.ca; liju@mit.edu; zhiyuzeng@cityu.edu.hk

Sections

Introduction

Intercalation strategies

Effects of intercalation

In situ studies of intercalation

Outlook

Introduction

Within just a few years of the discovery of graphene in the early 2000s¹, 2D materials became an area of great interest for materials researchers. These 2D materials revolutionized many aspects of current research, especially in emerging physics, opto-electronic devices, catalysis, batteries and more^{2–5}.

These materials feature anisotropic bonding – a strong covalent bond within the layers themselves and weak van der Waals (vdW) interactions between adjacent layers (Fig. 1a). This anisotropic nature makes intercalation in 2D materials feasible – the intercalated 2D materials are also known as artificial superlattices⁶. Here, intercalation refers to the insertion of foreign species (atoms^{7–9}, ions^{10–16} or molecules¹⁷) into the layer spaces (vdW gaps) of 2D materials^{7–13,15,17} (Fig. 1b) or their vdW heterostructures¹⁴ (Fig. 1c) – a vdW heterostructure is a novel heterostructure in the form of vdW stacks, created by stacking different 2D crystals vertically with one-atomic-plane precision¹⁸.

After intercalation, the interlayer adhesion declines, facilitating the isolation of atomic layers¹⁹. This makes intercalation a tool for the exfoliation synthesis of atomically thin materials¹⁹ (2D nanosheets and 1D nanoribbons, see Boxes 1 and 2, respectively). Crucially, it is also a powerful part of the property-tuning toolkit of 2D materials^{20,21}. Intercalation brings synergistic effects between layers and guests, triggers the changes in interlayer interactions and induces charge (electron or electron hole) transfers, which result in changes in the in-plane bonding configurations, Fermi energies, electronic band structures and spin–orbit effects. These effects tune the properties of 2D materials in various fields from photonics, electronics, optoelectronics, thermoelectricity, magnetism, catalysis and energy storage.

Intercalation in 2D materials has been the topic of several previous review articles^{6,19–24}, with contents covering intercalation for tuning the physics and chemistry of 2D materials^{6,20,21}, applications in electronics, optoelectronics, magnetic, energy storage and more^{20,21,23} and for exfoliations of 2D materials^{19,22,24}. The current article aims at providing an updated perspective on advancements from an atomic and intrinsic mechanism, while offering an overview towards the state-of-the-art in situ techniques for study intercalation mechanisms. The discussions of this article focus on intercalation in atomically thin 2D vdW materials (such as bi-layer graphene and few-layer MoS₂) – intercalation in thick layered materials or restacked 2D material membrane (such as MXenes electrode) is not included and readers can refer to several previous articles for this^{25–28}.

In this Review, we first discuss intercalation strategies, before we present the atomic and intrinsic effects of intercalation in 2D materials. Following this, examples of in situ studies of intercalation in 2D materials are given. Finally, thoughts and directions for the future of intercalation in 2D materials are detailed.

Intercalation strategies

To achieve intercalation, the intercalated compound should be thermodynamically more stable than the physical mixture of the foreign species and 2D materials in a given environment; otherwise, deposition occurs instead⁶ (Fig. 1d). In parallel, the insertion of foreign species also requires that a certain energy barrier must be overcome, which is related to the interlayer interactions of 2D materials and the diffusion coefficients of the guest species⁶.

The overall intercalation strategies can be divided into chemical^{9,11,17} (Fig. 1e) and electrochemical^{10,12–15} (Fig. 1f) intercalation. Chemical intercalation can be solution-based^{9,11,17} or in the vapour phase^{29–32}, whereas electrochemical intercalation can apply liquid^{4,13,15} or solid electrolytes^{10,12,14} – demonstrating the diversity of intercalation strategies. Here, we briefly introduce these intercalation strategies, discuss the basic processes and suitable species and highlight the key advantages and limitations of each method. For a comparison of the intercalation strategies, see Table 1. For additional information about the intercalation strategies, the reader is referred to several previous review articles^{6,20,21,23,33}.

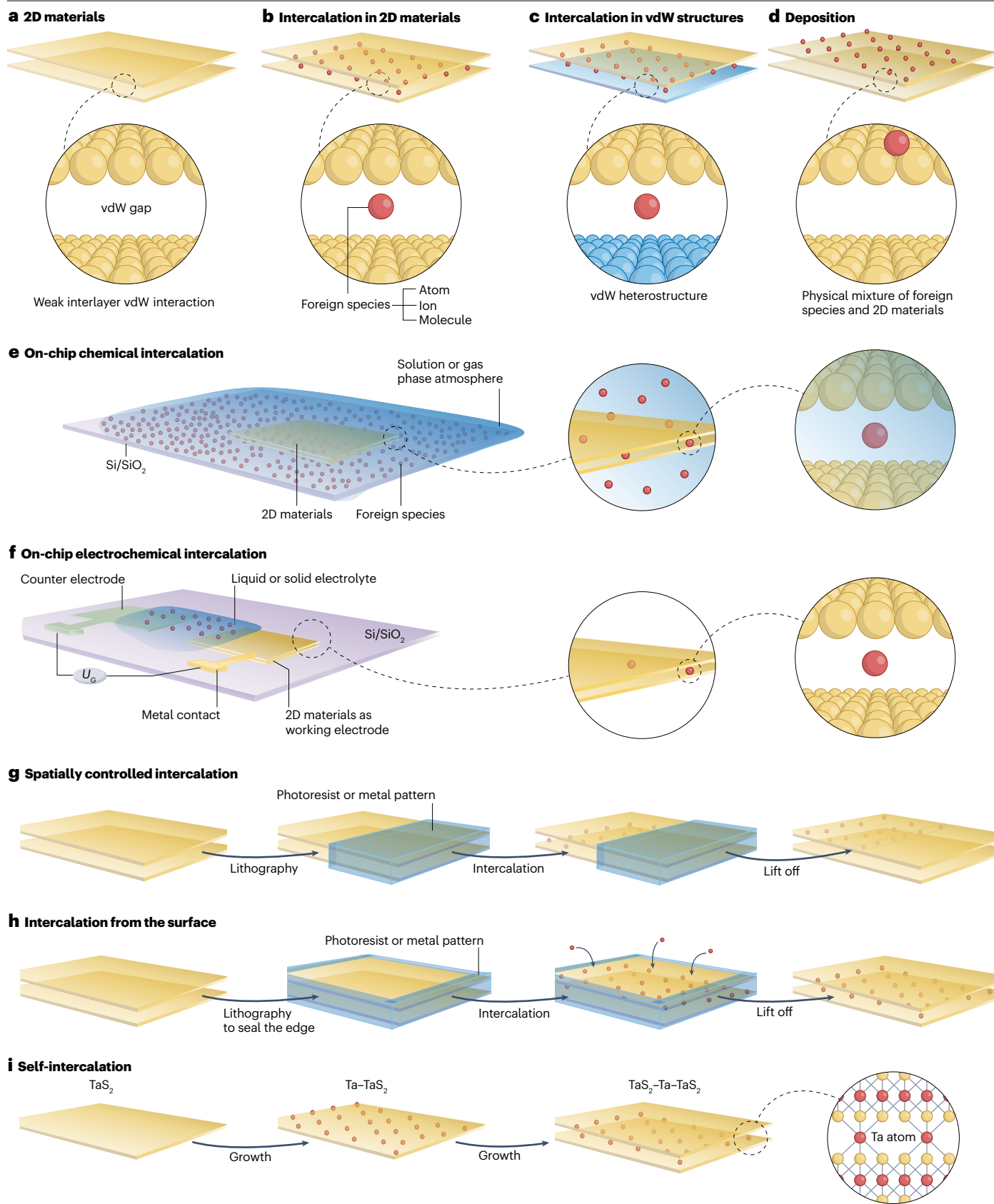
Chemical intercalation

Solution-based chemical intercalation can be achieved by simply immersing on-chip 2D materials in an intercalant solution^{9,11,17}. Such an intercalation process is driven by the concentration gradient of the solution-based species foreign to the layered material and follows diffusion kinetics. Usable intercalant species include atoms (such as copper and cobalt)⁹, ions (such as lithium ions)¹¹ and molecules (such as chiral molecules)¹⁷. This is usually a spontaneous or low-temperature heat-assisted process – but time-consuming – normally ranging from a few hours to a few days. A large chemical potential difference between the foreign species and the 2D materials can accelerate intercalation³⁴. But, excessive chemical potential differences may also lead to a chemical decomposition onto the 2D materials¹⁹.

Vapour-phase chemical intercalation normally operates at high temperatures in an enclosed vessel, exposing on-chip 2D materials to the vapourized intercalants^{29–32}. This intercalation process can be isothermal³¹ or achieved through a two-zone (with temperature gradient) transport mechanism³². Atoms (such as Ta)⁸, ions (such as oxygen plasma, which contains O₂⁺ and O⁺)²⁹, molecules (such as FeCl₃)³² and many more can all be intercalated in this way. This intercalation process can generally be completed in several hours, demonstrating its time-saving advantage. However, the harsh intercalation condition (high temperatures) is a shortcoming. In addition, vapour-phase chemical intercalation usually needs to be performed in an inert environment to avoid thermally oxidizing the 2D materials, also contributing to the drawbacks of this technique.

Fig. 1 | Intercalation in 2D materials. **a**, A schematic illustration of 2D materials with weak van der Waals (vdW) interactions between adjacent layers. **b**, Foreign species intercalated between the 2D layers could be atoms, ions or molecules. **c**, Beyond 2D materials, intercalation can also happen in their vdW heterostructures. **d**, Deposition is favoured over intercalation when the intercalated compound is less thermodynamically stable than the physical mixture of the foreign species and 2D materials in a given environment. **e**, Chemical intercalation occurs by immersing 2D materials into an intercalant solution or exposing it to vapourized intercalants. **f**, Electrochemical intercalation normally runs on an on-chip electrochemical cell, in which the

targeted 2D material is a working electrode and connects with a patterned metal contact. A counter electrode and electrolyte containing the ionic intercalants complete the electrical circuit. U_c , voltage. **g**, Spatially controlled intercalation is achieved by locally wrapping the 2D materials (through photoresists or metal pattern), followed by an intercalation process before the wrap is lifted off (removal of photoresist or metal pattern). **h**, When the edges of 2D materials are fully sealed by photoresists or metal pattern, small atoms or ions may intercalate into the vdW gaps of 2D materials from the top surface. **i**, Self-intercalation is when the intercalation species is a native atom rather than foreign, such as tantalum (Ta) intercalation into 2D tantalum disulfide (TaS₂).



Electrochemical intercalation

Electrochemical intercalation is typically performed on an on-chip electrochemical cell^{10,12–15}. The targeted 2D material is a working electrode and its edges are connected with a patterned metal contact ('patterned' here means making the metal contact with a specific shape and coverage area), which is deposited via electron-beam lithography or a mask evaporation process. A metal counter electrode and an electrolyte containing the ionic intercalants are also required to complete the electrical circuit. Applying a voltage to the two electrodes creates a potential gradient between them, which drives the movement of ionic intercalants, achieving intercalation.

The rate and degree of intercalation can be controlled by adjusting the applied voltage or current passing through the circuit²⁴. This process can be monitored by following the voltage profile²⁴. Intercalation and de-intercalation can usually be switched as desired by controlling the charge–discharge conversion^{13,35,36}. Rapidity, controllability and switchability are the considerable advantages of electrochemical intercalation. To date, these advantages make it the most popular and widely used intercalation method, particularly appealing in devices involving electrostatic gating^{6,10,37} – also known as electrostatic doping, referring to the replacement of donor/acceptor dopants with gate-induced free charges (electron/hole) – and rechargeable batteries^{38,39}.

Box 1

Intercalation as a tool for the synthesis of 2D nanosheets

As mentioned, intercalation can increase interlayer distances and weaken interlayer adhesion (van der Waals force), facilitating the isolation of atomic layers¹⁹. This makes intercalation a powerful tool for the exfoliation of 2D nanosheets from their bulk^{19,24,40,63} – 2D nanosheets are sheet-like atomically thin materials. The typical procedure for this strategy involves the intercalation of foreign species, followed by a mild sonicating exfoliation. To obtain pure 2D sheets, a subsequent centrifugal washing treatment is typically required. Such treatments involve a low-speed (such as 2,000 rpm) centrifugal process to remove large chunks and high-speed (such as 10,000 rpm) centrifugation with multiple cycles to release the intercalation agents and solvents. Following this, the collected 2D-nanosheets-rich sedimentation (pure 2D sheets) is often redispersed in solvents (such as water, acetone, isopropyl alcohol, dimethyl sulfoxide and *N,N*-dimethyl formamide) via a mild sonication step for later functional applications.

Lithium ions (Li⁺) are a famous intercalation species for synthesizing 2D nanosheets^{24,153–155}. The intercalation of Li⁺ can be achieved via a chemical^{153,154} or electrochemical route^{24,155}. Several types of Li⁺ intercalants are available for the chemical intercalation process, including *n*-butyllithium (*n*-BuLi) (refs. 89,154), lithium borohydride (LiBH₄) (refs. 156,157), naphthalene lithium (Nap-Li) (ref. 158) and pyrene lithium (Py-Li) (ref. 34). These intercalants are mainly used to exfoliate transition metal dichalcogenide (TMD) materials, resulting in the synthesis of monolayers with high yield, but the resultant nanosheets often differ structurally and electronically from their bulk counterparts (known as structural phase transition: the phase transfer from 2H to 1T or 1T') (ref. 19). The drawbacks for most of the chemical Li⁺ intercalation process also lie in the long time (2–3 days) and harsh conditions (100–300 °C, argon-filled glovebox).

Alternatively, electrochemical Li⁺ intercalation is relatively rapid and mild^{24,155,159–161} – achievable within 6 h at room temperature. The degree of Li⁺ insertion in the electrochemical Li⁺ intercalation-based exfoliation strategy is easily controlled by tuning the cut-off voltage²⁴. This avoids poor exfoliation efficiency and crystal structure decomposition caused by incomplete and excessive Li⁺ insertion, respectively²⁴. This strategy is also generic. It achieves high-yield production of diverse monolayer or few-layer inorganic nanosheets, including graphene¹⁵⁵, hexagonal boron nitride¹⁵⁹,

various TMDs^{24,155,159,161}, Sb₂Se₃ (ref. 159), Bi₂Te₃ (ref. 159) and Pd₃P₂S₈ (ref. 160). In spite of the aforementioned advantages, the 2H to 1T or 1T' phase transition of the final products is still difficult to avoid for this method¹²⁴.

Using large-sized tetraalkylammonium ions (R₄N⁺, such as tetraheptylammonium ions) as intercalation species solves the problem regarding phase transitions, ultimately resulting in 2D nanosheets of high purity⁴⁰. The large size of R₄N⁺ naturally limits the number of intercalated ions into the layer space of bulk TMD materials and thus reduces the transfer number of electrons from intercalated ions to the *d* orbitals of the host transition metal atoms, bypassing the phase transition⁴⁰. Intercalation with R₄N⁺ is carried out in an electrochemical cell with a bulk crystal cathode, Pt wire (or foil) anode, and an R₄N⁺-containing electrolyte. Following the successful synthesis of high-quality MoS₂ nanosheets with a high-purity 2H phase⁴⁰, a range of other 2D nanosheets have been prepared by the R₄N⁺ intercalation-based exfoliation strategy from graphene¹⁶² to other TMDs^{40,63,163–165}, black phosphorus^{166–169}, A₂B₃ (such as In₂Se₃ (refs. 40,170,171), Bi₂Se₃ (ref. 40) and Sb₂Te₃ (ref. 40)), to materials with a formula of AMX₂ (such as AgCrS₂)¹⁷². Normally, exfoliated nanosheets are solution-processable, printable and compatible with various solution-based deposition techniques (such as drop casting, inkjet printing and industrial roll-to-roll coating)¹⁹. These properties make it easy to integrate the final product into various substrates (such as Si or SiO₂ and porous polymers), leading to the manufacture of customizable devices, such as high-performance MoS₂ transistors^{40,173,174} adaptable and breathable electronic membranes¹⁷⁵. The current drawbacks of using R₄N⁺ for intercalation strategies are its high cost and its resulting low single-layer yield.

Beyond Li⁺ and R₄N⁺, other intercalation species are also used to peel off nanosheets, such as sulfate ions (SO₄²⁻)¹⁷⁶, boron tetrafluoride ion (BF₄⁻)¹⁷⁷ and small molecules (such as 4,4'-dipyridyl disulfide¹⁷⁸ and alkylamine¹⁷⁹). Additionally, the quality of the exfoliated nanosheets is influenced by several factors, including the types and concentrations of the intercalant, polarity, surface energy (surface tension) and Brønsted–Lowry acidity of the solvent, magnitude and duration of the applied voltage and the exfoliation power¹⁹. For additional information about the intercalation-based exfoliation strategy for the synthesis of 2D nanosheets, the reader is referred to ref. 19.

Box 2

Intercalation as a tool for the synthesis of 1D nanoribbons

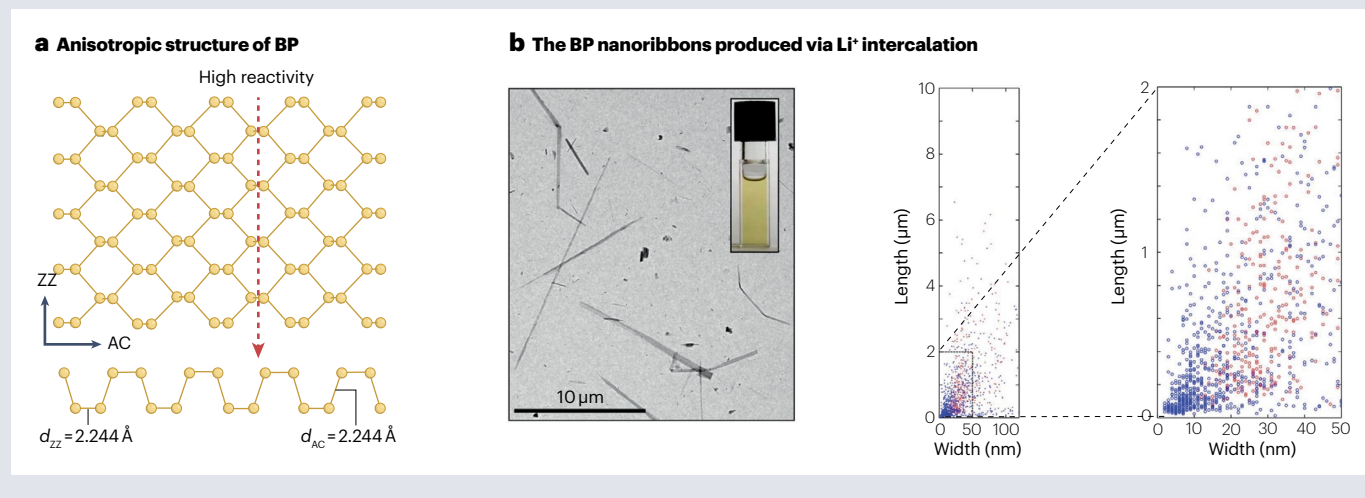
Beyond the synthesis of 2D nanosheets, intercalation has also been applied for the fabrication of 1D nanoribbons, especially black phosphorus (BP) nanoribbons^{180–184} — 1D nanoribbons are ribbon-like atomically thin materials characterized by a large aspect ratio. The BP crystal has anisotropic in-plane bond energies, owing to its non-equivalent P=P covalent bonds along the armchair (AC, $d_{ac}=2.224\text{ \AA}$) direction and zigzag (ZZ, $d_{zz}=2.244\text{ \AA}$) direction¹⁸⁵ (see the figure, panel **a**). When small ions are intercalated into the layer space of BP crystals, small lattice strains will occur in BP. Such strains tend to create a fissure along the ZZ direction, resulting in the exfoliation of BP like a zipper, ultimately forming BP nanoribbons¹⁹.

The famous Li^+ has been reported as the intercalation species for the synthesis of 1D BP nanoribbons^{180,181}. The fabrication process starts with an outgassing treatment of BP crystals at 100°C under dynamic vacuum for 1 week, followed by several steps in series, including mixing of BP-layered crystal and lithium metal, a cooling treatment (-50°C), a lithium-dissolving process via adding ammonia gas, an Li^+ intercalation process (24h), an ammonia-removing treatment and a drying process of the intercalation compound. The process ends with an exfoliation treatment via sonication (1h) or stirring (1 week) by adding anhydrous aprotic solvent. Stable, uniform and flexible BP monolayer nanoribbons could be fabricated by this method (see the figure, panel **b**, whose left part presents a transmission electron microscopic image of the obtained BP nanoribbons and the photograph of the BP suspension and the right part shows the length versus width scatterplots and the corresponding enlarged view of the BP nanoribbons, extracted from transmission electron microscopic data). But this strategy is constrained by its complex, time-consuming and environmentally demanding natures.

The 1D BP nanoribbons can also be fabricated via an electrochemical BF_4^- intercalation-based exfoliation strategy¹⁸³. The overall process involves electrochemical BF_4^- intercalation and oxygen-driven exfoliation. The electrochemical intercalation is performed in an electrochemical cell with bulk BP anode, platinum (Pt) cathode and $[\text{BMIM}]\text{BF}_4$ water solution as an electrolyte. This method is simple and feasible, avoiding the drawbacks of the aforementioned chemical Li^+ intercalation-based exfoliation method. But, the disadvantage of this method lies in the impact of oxygen molecules towards the final products, which results in impure BP nanoribbons, containing lots of neutral defects and dangling oxygen and hydrogen bonds at the edges.

Using TPA^+ (ref. 184) or Na^+ (ref. 182) as intercalation species is also feasible for the fabrication of 1D BP nanoribbons. The typical procedure of this method involves an electrochemical cation intercalation and a subsequent sonication exfoliation process. The two-electrode electrochemical cell is applied for the TPA^+ intercalation process, with a bulk BP crystal cathode, Pt wire (or foil) anode, and TPA^+ -containing electrolyte¹⁸⁴. Electrochemical Na^+ intercalation was performed in a coin cell with BP crystal cathode, Na metal anode and sodium hexafluorophosphate (NaPF_6) in ethyl carbonate and propylene carbonate mixture solution as electrolyte¹⁸². The overall process is carried out in an argon-filled glovebox, thereby avoiding the impact of oxygen. The final BP nanoribbons, therefore, are high purity without neutral defects (small widths: $10.3\pm 3.8\text{ nm}$ and short lengths: $250\pm 156\text{ nm}$), dangling oxygen and hydrogen bonds.

Panel **b** is reprinted from ref. 180, Springer Nature Limited.



The limitation of this intercalation technique lies in the requirement for charged intercalants — but it is highly efficient for most ion intercalation species (such as lithium ions (Li^+)^{10,12–14}, cetyl-trimethylammonium

ions (CTA^+)¹⁵ and tetraalkylammonium ions (R_4N^+)⁴⁰). In addition, it is necessary to ensure that the 2D materials are electrochemically stable within the applied voltage window.

Table 1 | A comparison of different intercalation strategies

Strategies	Suitable species	Advantages	Disadvantages	Examples
Solution-based chemical intercalation	Atoms (such as Cu and Co) ⁹ , ions (such as Li ⁺) ¹¹ , molecules (such as chiral molecules) ¹⁷	Easy to process, reversible, scalable, clean product (no SEI), high degree of intercalation, available to all host materials (include non-conductive ones)	Slow kinetics, time-consuming (from hours to days), hard to precisely control the concentration of intercalants, hard to achieve real-time characterization	Cu and Co intercalation in SnS ₂ (ref. 9); Li ⁺ intercalation in MoS ₂ (ref. 11); R- α -methylbenzylamine or S- α -methylbenzylamine intercalation in TaS ₂ and TiS ₂ (ref. 17)
Vapour-phase chemical intercalation	Atoms (such as Ta) ⁸ , ions (such as oxygen plasma, which contains O ₂ ⁺ and O ⁻) ²⁹ , molecules (such as FeCl ₃) ³²	A little fast (several hours), scalable, available for most of host 2D materials (including non-conductive ones), product without contamination	Harsh in intercalation conditions (high-temperature and inert gas atmosphere), low controllability, hard to achieve real-time characterization	Ta intercalation in TaS ₂ (ref. 8), oxygen plasma, containing O ₂ ⁺ and O ⁻ intercalation in MoS ₂ (ref. 29), FeCl ₃ intercalation in graphene ³²
Electrochemical intercalation	Ions (such as Li ⁺ (refs. 10,12–14), CTA ⁺ (ref. 15), R ₄ N ⁺ (ref. 40))	Fast in speed, controllable for the intercalation process and switchable between the intercalation and de-intercalation, scalable, available for real-time characterization	Not workable for electroneutral atoms and molecules, sometimes unclean in product (with SEI), host 2D materials need to be conductive	Li ⁺ intercalation in MoS ₂ , TaS ₂ , bilayer graphene and hBN-MoS ₂ -graphene-hBN heterostructures ^{10,12–14} , CTA ⁺ intercalation in BP ¹⁵ , R ₄ N ⁺ intercalation in MoS ₂ , WSe ₂ , Bi ₂ Se ₃ , NbSe ₂ , In ₂ Se ₃ and Sb ₂ Te ₃ (ref. 40)
Spatially controlled intercalation	Atoms (such as Cu and Co) ⁹ , ions (such as Li ⁺ and H ⁺) ^{11,30,41}	Spatially controllable for intercalation	Requires both intercalation and lithography techniques	Cu and Co intercalation in SnS ₂ (ref. 9), Li ⁺ intercalation in MoS ₂ (ref. 11), H ⁺ intercalation in MoO ₃ (ref. 30)
Intercalation from the surface	Small atoms or ions (such as Li ⁺ and Na ⁺) ³⁵	Uniform intercalation of foreign species	Only feasible for small atoms or ions	Li ⁺ intercalation from MoS ₂ surfaces ³⁵
Self-intercalation	Atoms (such as Ta (ref. 8) and Cr (refs. 43,48–50))	High-quality products, well-defined phases, long-range crystalline order	Harsh intercalation conditions (high temperature and high native atom flux)	Self-intercalation of Ta in TaS ₂ (ref. 8), the self-intercalation of Cr in CrS ₂ (refs. 43,48–50)

BP, black phosphorus; CTA⁺, cetyl-trimethylammonium ion; hBN, hexagonal boron nitride; R₄N⁺, tetraalkylammonium ion; SEI, solid electrolyte interface.

Emerging intercalation techniques

New forms of intercalation are emerging, such as spatially controlled intercalation^{9,11,30,41}, intercalation from the surface^{35,42} and self-intercalation^{8,43–45}.

Spatially controlled intercalation (Fig. 1g) is a fascinating process that enables spatial and size control of the intercalation process and can produce in-plane heterostructures^{9,11,30,41} – formed through lateral interfacing of atomic layers of different materials, which is opposite to the vertical heterostructure created by the layer-by-layer stacking of atomic layers of different materials⁴⁶. Spatial and size control is achieved via a local ‘masking’ strategy, which can be applied by a patterned metal deposition (such as zinc and aluminium)⁹ or with a photoresist coating^{11,30}, followed by lithography^{9,11,30}. After intercalation, a chemical etching process normally follows to remove the metal or photoresist. Although this intercalation approach enables spatial and size control, it is highly reliant on micro–nano masking technology involving lithography, increasing the technical difficulty of implementation.

Intercalation from the surface (Fig. 1h) refers to the insertion of foreign species into the vdW gaps from the surface of 2D materials rather than from the edges; normally, intercalation from the edges shows less intercalation resistance and more prone to occur^{35,42}. Surface intercalation occurs when the edges of the 2D materials are fully encapsulated by metal or other encapsulating agents³⁵. Normally, only small atoms or ions are used for such intercalation. For example, Li⁺ and Na⁺ can pass through the top surface of MoS₂ into its vdW gaps, but larger-sized K⁺ cannot³⁵. This is because the surfaces of 2D materials are covalently

bonded – in principle, foreign species can only enter the vdW gaps through the limited atomic gaps. However, surface vacancies create surface entrances large enough for small ions to penetrate leading to uniform intercalation³⁵. By contrast, the lateral intercalation (intercalation from the edges to the centre) is normally a continuous and gradual process, forming distinct intercalated and non-intercalated domains⁴⁷.

Self-intercalation (Fig. 1i) refers to the insertion of native atoms (for example, Ta intercalation in 2D TaS₂ (ref. 8) and Cr intercalation in 2D CrTe₂ (refs. 43,48–50)), as opposed to foreign atoms. Owing to the close chemical potential between native atoms and the target 2D materials, self-intercalation is difficult to achieve through the traditional intercalation methods, which are post-insertion and diffusion-limited processes. A feasible strategy for self-intercalation is to embed native atoms in the 2D materials during the layer-growing process by increasing the native atom flux^{8,43–45,51}, in which both molecular beam epitaxy and chemical vapour deposition are useful techniques⁸. The superiority of self-intercalation (compared with traditional intercalation strategies that involve the intercalation of foreign species) lies in the high quality of its products, which often have a well-defined intercalated phase with long-range crystalline order with ferromagnetic properties^{8,48,49}, which are difficult to obtain by traditional intercalation ways.

Effects of intercalation

Intercalation can, among others, lead to synergistic effects, changes to interlayer interactions, reconstructions of in-plane bonding, shifts of Fermi levels, changes in electronic band structures, tuning of the spin–orbit effects and lattice parameters. Here, we introduce the effects

resulting from intercalation, highlighting their tuned properties and the corresponding applications in Supplementary Table 1.

Synergistic effects

These effects often appear in intercalated 2D materials (the so-called artificial superlattices), granting them properties beyond the reach of simpler, non-intercalated materials^{17,52}.

The synergistic effect between the 2D crystals and intercalant is reflected in the following two aspects. On the one hand, intercalation species can inject new properties into 2D crystals, which are usually absent in the pure material. On the other hand, the atomic layers of the 2D crystals provide protection for the intercalation species, protecting them from damage during applications.

A prominent example is 2D tin disulfide (SnS₂) intercalated with catalytically active metal single atoms (such as Pt, Pd, Ni and Cu), which shows outstanding catalytic performance and superior long-term durability⁵² (Fig. 2a). The metallic single atoms endow the intercalation compound with catalytic activity, whereas the atomic layers of 2D SnS₂ protect the catalytic centres by confining them within the layers, endowing the compound with ultrahigh electrocatalysis stability (no conspicuous decay of the current after 72 h tested at a current density of 10 mA cm⁻² (ref. 52) compared with the physically adsorbed single-atom catalysts (stable for <24 h at a current density of 10 mA cm⁻² (ref. 53)). Such a metal single-atom intercalated 2D crystal is a promising candidate for catalysts of the future, achieving high atom efficiency and superior durability.

Intercalating chiral molecules (for instance, R- α -methylbenzylamine or S- α -methylbenzylamine) into 2D atomic crystal (such as TaS₂ and TiS₂) make the created artificial superlattices exhibit chiral-induced spin selectivity, broadening its application for spintronic devices without external magnetic fields¹⁷ (Fig. 2b) – a semiconductor device in which spin properties are introduced, using electron charge and spin together as the carrier of information. The 2D atomic crystal has electronic conductivity and the ability to integrate into functional devices and to give protection to chiral molecules.

Inserting paramagnetic ions (such as holmium⁵⁴ and/or iron ions⁵⁵) into 2D crystal endows the superlattice with an active magnetic response, which is a novel method for creating promising magnetic devices capable of processing and storing information. The magnetic response can be tuned by controlling the concentration of intercalated paramagnetic ions, and a rapid reversal of the magnetic response can be achieved by de-intercalation⁵⁴.

Despite the synergistic effects in an intercalated compound, the opposite can also be true where adverse effect presents themselves as reflected in the two following aspects. On the one hand, the confinement of atomic layers of a 2D material may prevent the properties of intercalated species from being fully utilized. For example, when conducting catalytic high-value reactions of biomass macromolecules, 2D artificial superlattices intercalated with catalytically active metal single atoms may exhibit catalytic inertness. This is due to a lack of physical access between the biomass molecules and the catalytically active metal – blocked internally and externally by the atomic layers. By contrast, the intercalation of foreign species may damage the 2D material, weakening or even removing their original properties. For instance, the intercalation of alkali metal ions often results in the phase transition of 2D transition metal dichalcogenides (TMDs) from the semiconducting 2H phase to the metallic 1T phase^{11,13,19,24} (a detailed discussion concerning phase transitions is present in the ‘Reconstructing in-plane bonding’ section). Further to this, the intercalation of sulfate

ions (SO₄²⁻) may oxidize multiple layers of graphene⁵⁶ or introduce lattice defects in 2D TMDs⁵⁷, thereby weakening the electronic conductivity of the original graphene and TMDs.

Therefore, to create an artificial superlattice through intercalation with ideal synergistic effects and no inhibitory effects, a reasonable selection of the 2D host crystals and guest species is crucial. Machine learning will be a powerful tool to drive this selection⁵⁸, and through it intercalation can be modelled, guiding researchers in designing and synthesizing new intercalated artificial superlattices as needed.

Changes in interlayer interactions

Intercalation often triggers *c*-axis lattice expansion^{15,59,60} (Fig. 2c). For example, oxygen plasma (containing O₂⁺ and O⁻) intercalation increases the interlayer distance of MoS₂ from 6.05 Å to 9.27 Å (ref. 29). Larger lattice expansions present themselves when long-chain organic ions (such as CTA⁺ (refs. 15,40,61) and tetrabutylammonium ions^{62,63}) are the intercalants. After CTA⁺ intercalation, the interlayer distance increases from 5.23 Å to 11.27 Å in 2D black phosphorus (BP) and from 6.16 Å to 15.09 Å for 2D MoS₂ (ref. 15).

Lattice expansion can weaken the interlayer interaction in 2D materials, which may lead to various changes to its properties including the generation of natures that are intrinsic to monolayer materials^{15,29,62,64–66}, phonon scattering^{67–69}, enhancing the degrees of freedom for interlayer sliding⁷⁰ and reducing cross-plane thermal conductivity along with improving electron mobility in the compound⁷¹.

Weakening interlayer interactions can result in the appearance of exotic properties (that are intrinsic to monolayer materials) in intercalated 2D materials^{15,29,62,64,65}. These exotic properties include photoluminescence²⁹, superconductivity⁶⁴, ferromagnetism⁶² and more (as discussed in this section). Impressively, the properties exhibited in the artificial superlattices often surpass those shown in their monolayer counterparts²⁹. Also, owing to the mutual protection of adjacent layers, intercalated 2D materials are more stable in air than similar, but non-protected monolayer materials^{15,65}.

For example, the MoS₂[O₂]_x artificial superlattice created via soft oxygen plasma intercalation has a bandgap similar to what is intrinsic for an MoS₂ monolayer²⁹ (Fig. 2d). Photoluminescent properties have also been reported for this material, which is almost 100 times stronger than that of MoS₂ monolayers on their own²⁹ – this could open the door for new optoelectronic developments of TMDs.

The 2D BP superlattice produced by CTA⁺ intercalation exhibits a bandgap of 2.13 eV, close to that of a BP monolayer (1.94 eV)¹⁵ (Fig. 2e). The superlattice allows access to the key properties of BP monolayer, from high carrier mobility to high on/off current ratio and to large optical bandgap¹⁵ (optical bandgap is a solid-state physics term, representing the energy difference between the lowest point of the conduction band and the highest point of the valence band) – but the superlattice also allows for superior environmental stability with less BP degradation, which is otherwise flammable¹⁵. This stable superlattice is the future of functional BP electronics and optoelectronics.

Additionally, intercalation in topological insulators (also called quantum spin Hall insulators such as Bi₂Se₃, Bi₂Te₃ and Sb₂Te₃) may result in superconductivity⁶⁴. Topological insulators are a class of materials that are insulated internally (in the bulk), but show metallic (conductive) behaviour on its surfaces. Weakening the interlayer interactions owing to intercalation can make the surface conductance of a topological insulator more dominant, leading to superconductivity⁶⁴. Furthermore, intercalation induces topological transitions from an initial type-II Weyl semimetal of orthorhombic MoTe₂ and WTe₂ to a

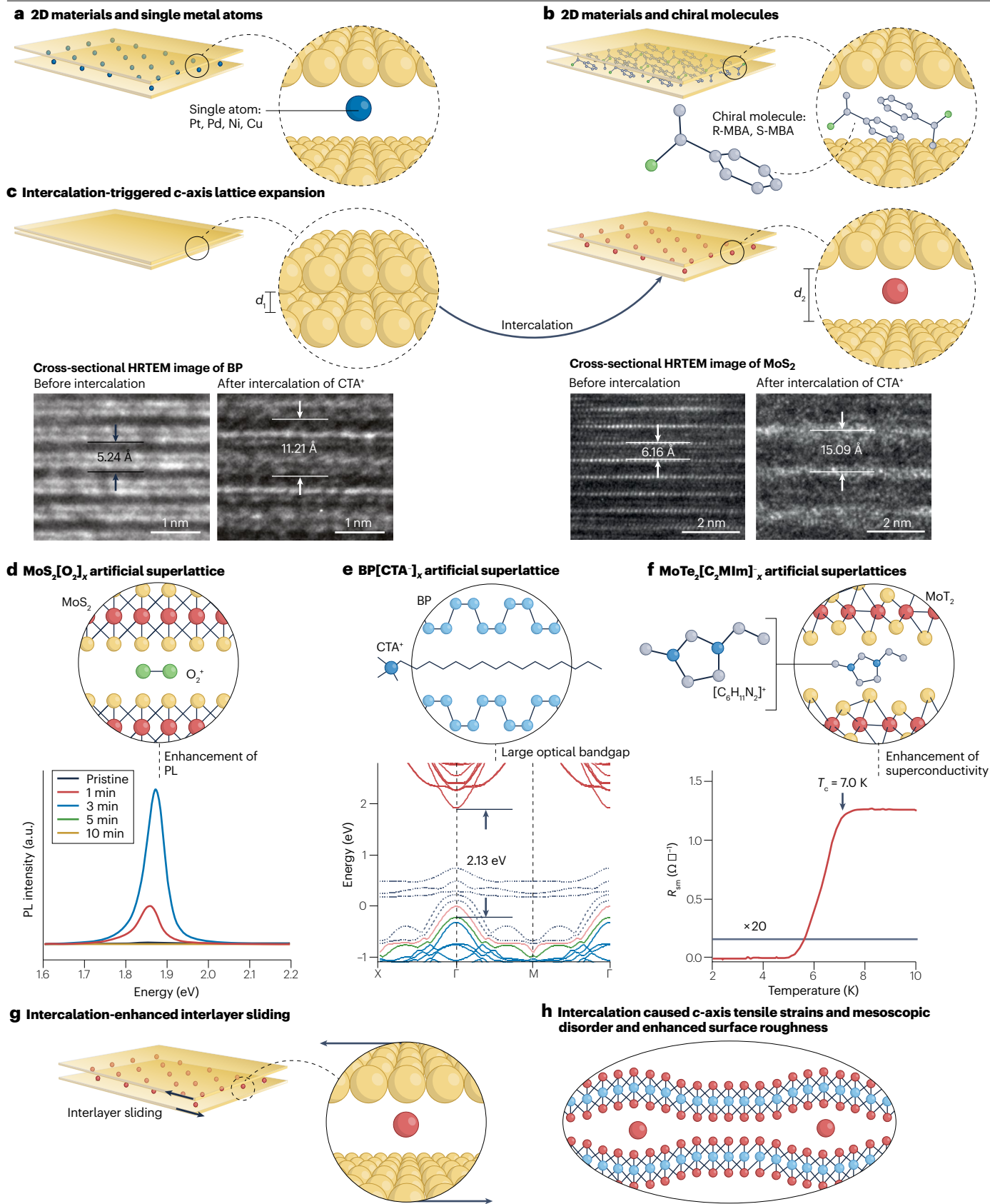


Fig. 2 | How intercalation can bring synergistic effect and change interlayer interaction.

a, Synergistic effects between 2D materials and single metal atoms (such as Pt, Pd, Ni and Cu). **b**, Synergistic effect between 2D materials and chiral molecular (R- α -methylbenzylamine (R-MAB) or S- α -methylbenzylamine (S-MAB)). **c**, Following intercalation, the interlayer distances increase ($d_2 > d_1$). For example, after cetyl-trimethylammonium ion (CTA⁺) intercalation, the interlayer distance increases from 5.24 Å to 11.21 Å for 2D black phosphorus (BP) and from 6.16 Å to 15.09 Å for 2D molybdenum disulfide (MoS₂) as seen in the high-resolution transmission electron microscopic (HRTEM) images. **d**, MoS₂[O₂]_x artificial superlattice (top part) and its strong photoluminescence (PL) property (bottom part). The bottom part is the time-dependent PL spectra of pristine MoS₂ (non-intercalated) and plasma-treated (O₂⁺ intercalated) MoS₂, demonstrating strong PL of 3-min plasma-treated (O₂⁺ intercalated) MoS₂. **e**, BP[CTA⁺]_x artificial superlattice (top part) and its large optical bandgap (bottom

part). The bottom part is the simulated electronic structure of BP[CTA⁺]_x, showing the enlarged optical bandgap of 2.13 eV. Valence band maximum, green line; conduction-band minimum, red line. **f**, MoTe₂[C₂MIm]_x artificial superlattice (top part) and its enhanced superconductivity (bottom part). The bottom part is the low-temperature transport measurement of MoTe₂[C₂MIm]_x, demonstrating that its zero resistance temperature is about 5.1 K, meaning that it becomes superconducting at low temperature. MoTe₂, molybdenum ditelluride. The chemical formula of [C₂MIm]⁺ is [C₆H₁₁N₂]⁺. **g**, Intercalation-enhanced interlayer sliding. **h**, Intercalation causes *c*-axis tensile strain, mesoscopic disorder and enhanced surface roughness. a.u., arbitrary unit. Panel **c** is adapted from ref. 15, Springer Nature Limited. Panel **d** is adapted from ref. 29 under a Creative Commons licence CC BY 4.0. Panel **e** is adapted from ref. 15, Springer Nature Limited. Part **f** adapted with permission from ref. 65, Elsevier.

final topological insulator, altering their band structures which allow for superconducting properties⁶⁵ (Fig. 2f). Type-II Weyl semimetals (not following Lorentz symmetry) are one type of topological Weyl semimetals, and the other type, called type-I Weyl semimetals, follows Lorentz symmetry^{72,73}.

The weakening of interlayer interactions can enhance the degree of freedom of interlayer sliding and also reduce flexural modulus (making materials easier to bend), thereby improving structural flexibility⁷⁰ (Fig. 2g). Organic–inorganic superlattices, such as [(hexylammonium)_x(H₂O)_y(dimethyl sulfoxide)_z]/TiS₂, are emerging materials in the field of flexible wearable electronics⁷⁰.

An inhomogeneous distribution of intercalated species often leads to uneven *c*-axis lattice expansions, resulting in tensile strains along the same axis and mesoscopic disorder (high degree of surface roughness)⁶⁹. This induces phonon scattering, thereby reducing thermal conductance^{67–69} (Fig. 2h). These phenomena have been observed in 2D MoS₂ (refs. 67,69) and BP⁶⁸ with lithium electrochemically intercalated. Further to this, by switching between intercalation and de-intercalation (reversible intercalation), lattice expansions can be finely controlled and thereby the thermal conductance of 2D materials can be modulated, opening the door for creating switchable thermal transistors and laying the foundation for electrochemically driven thermal regulators of the future⁶⁹.

Beyond reducing thermal conductivity, the reduction of interlayer interactions (induced by a intercalation) may also improve or maintain electron mobility and electrical conductivity in the in-plane direction of 2D materials⁷¹. This endows intercalated material with the ability to generate thermoelectric power⁷¹, which is the notion of generating electricity from heat⁷⁰. A prominent example of this is the superlattice of alternating SnS and TiS₂, which displays enhanced thermoelectric properties compared with single, non-intercalated 2D TiS₂ materials⁷¹.

Although weakening the interlayer interactions caused by intercalation can result in the exotic properties of 2D materials as mentioned earlier, defects and potential issues remain. Owing to the weakening of interlayer interactions and the formation of lattice strain, intercalated 2D materials are easily broken during use^{19,74}. This problem may hinder the application of intercalated 2D materials in modern devices (such as large-area thin-film devices, transistors, photodetectors and optic modulators), which often rely on large 2D crystals (up to hundreds of microns). Performing a mild intercalation in a moderate environment (pH, current–voltage, intercalation agent concentration and temperature) by controlling the intercalation dynamics is a solution to this problem.

Reconstructing in-plane bonding

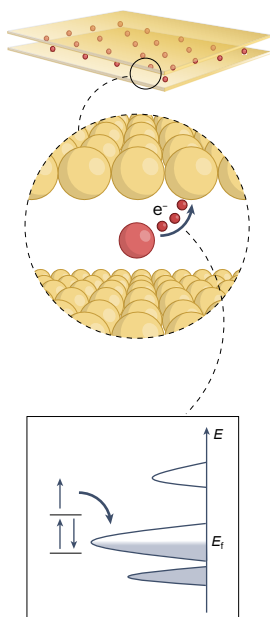
Intercalation can induce charge (electron or hole) transfers (Fig. 3a). Such transfers require a difference in chemical potential between the foreign species and 2D materials, in which the materials require the ability to accept electrons or holes. Alkali metal ions, particularly Li⁺, are commonly used as one-electron donors owing to their high reduction potential, whereas TMDs often only accept electrons owing to their negatively charged chalcogen layers⁷⁵. Spanning this divide is few-layer graphene, which can accept either electrons or holes during the intercalation process⁷⁶.

Intercalation-induced charge transfer can drive the reconstruction of in-plane bonding, resulting in structural phase transitions of 2D materials^{11,13,30,47,77–80}. Such transitions are particularly common in TMDs^{11,13,47}, whose general formula is MX₂, in which *M* and *X* refer to a transition metal and a chalcogen (S, Se and Te), respectively^{81,82}. TMD polymorphs exist with different coordination geometries of transition metal atoms^{81,82}: such as the 2H phase, which is a trigonal prismatic; the 1T phase, which is an octahedral; and the 1T' phase, which is a distorted octahedral (Fig. 3b). The stacking order within the atomic planes (*X–M–X*) differs between the polymorphs, in which the 2H phase exhibits Bernal stacking (ABA) and the 1T phase contains rhombohedral stacking (ABC). The diversity of the polymorphs and their structures give rise to various properties^{81,82} – for example, 2H-MoS₂ often show semiconducting properties, whereas 1T-MoS₂ and 1T'-MoS₂ can exhibit metallic and semimetallic characters, respectively. The three structures of these TMDs are close in energy owing to the small electronegativity of their chalcogens⁸³, which facilitates bond reconstruction in the TMDs under near-ambient conditions⁸³. This is why polymorphic phase transitions are common in TMDs.

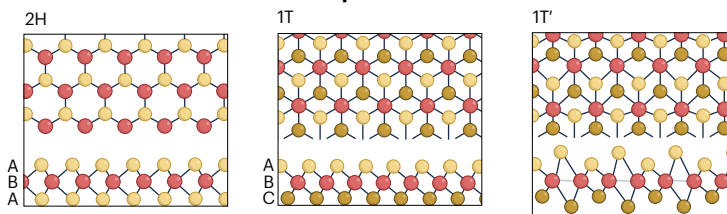
The intercalation of alkali metal ions, especially Li⁺, involves electron transfers from the *s*-orbital of alkali metal into the *d*-orbital of the host transition metal, becoming charge neutral overall. When electron transfer is beyond a certain threshold (for MoS₂, this threshold is 0.29 electrons per formula unit⁴⁰), the stability of the metal coordination of a trigonal prismatic structure (2H phase) will be lower than that of the octahedral structure (1T phase), and thereby the in-plane bond reconstruction and 2H-to-1T phase transitions occur (Fig. 3c). The octahedral coordination (1T phase) can spontaneously distort to form a distorted octahedral coordination structure (1T' phase). Therefore, the overall phase transitions of TMDs induced by the intercalation of alkali metal ions are 2H-to-1T/1T'.

Spatially controlled intercalation of alkali metal ions results in local 2H-to-1T/1T' phase transitions, producing in-plane TMD

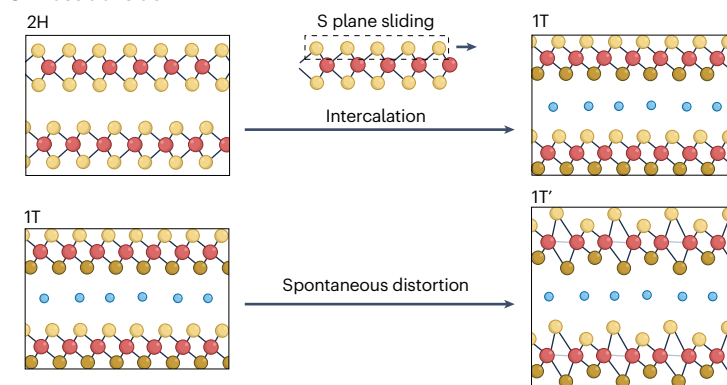
a Intercalation-induced charge transfers



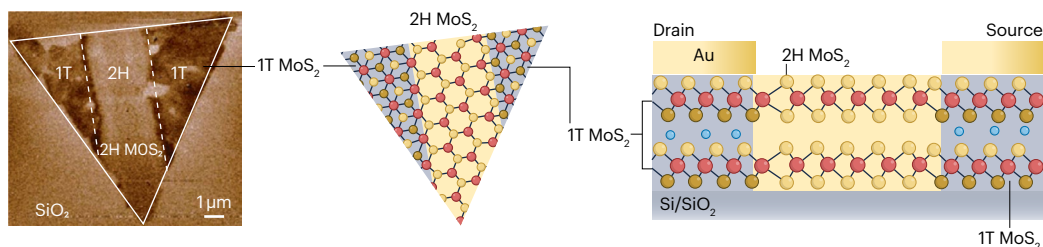
b Schematic models of various TMD phases



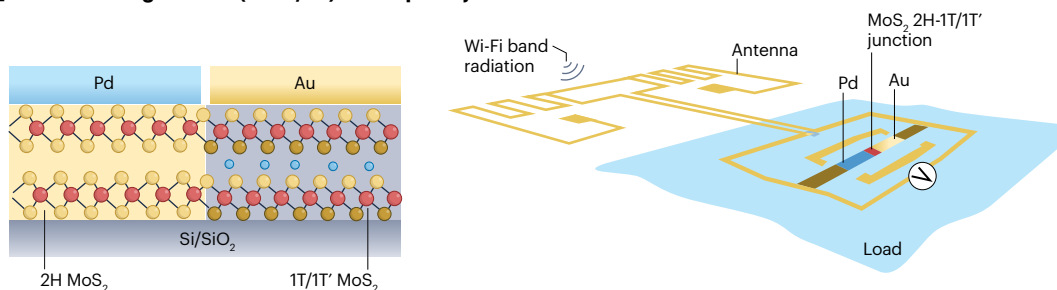
c Phase transition



d 1T-2H-1T MoS₂ hetero-phase junction (produced by local lithium-ion intercalation) and its transistor



e MoS₂ semiconducting-metallic (2H-1T/1T') hetero-phase junction and the fabricated flexible rectifier



f MoS₂-based memristive device and the coupled artificial neural networks

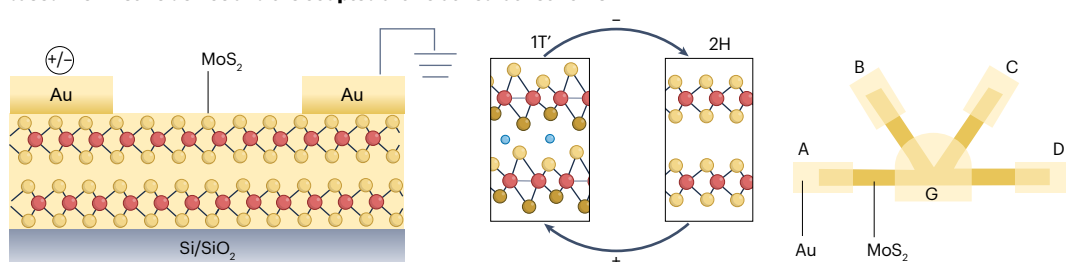


Fig. 3 | How intercalation can lead to reconstruction of in-plane bonding.

a, The bottom panel displays the electronic structure band diagram of the intercalation-induced charge transfers, as shown in the top of this panel. **b**, Schematic models of the different phases of transition metal dichalcogenides (TMDs). The 2H phase is trigonal prismatic, 1T phase is octahedral and 1T' phase is a distorted octahedral. Also shown are the stacking orders of the atomic planes for the 2H phase: Bernal stacking (ABA); the 1T phase and the rhombohedral stacking (ABC). **c**, 2H-to-1T and 1T-to-1T' phase transitions in TMDs during intercalation. **d**, The left part is the electrostatic force microscopic image of the prepared 1T-2H-1T molybdenum disulfide (MoS_2) hetero-phase junction. The middle part is the atomic model of this hetero-phase junction. The right part is the schematic illustration of the transistor with low-resistance contacts based on the 1T-2H-1T MoS_2 hetero-phase junction. **e**, The left part is the schematic illustration of the lateral Schottky diode based on the MoS_2 semiconducting-metallic (2H-1T/1T')

hetero-phase junction. The right part is a schematic of the flexible rectifier based on the MoS_2 semiconducting-metallic hetero-phase junction, integrated with a flexible Wi-Fi band antenna. **f**, The left part is a schematic illustration of the MoS_2 -based memristive device. In this device, one of the electrodes (right gold electrode) is normally grounded, and the voltage bias is applied on the other electrode (left gold electrode) to drive lithium-ion migration in the Li_xMoS_2 film. The middle part is an atomic model of a reversible phase transition in such memristive devices. When a negative voltage is applied to the left gold electrode, MoS_2 undergoes a 1T'-to-2H phase transition. When a positive voltage is applied to the left gold electrode, MoS_2 undergoes a 2H-to-1T' phase transition. The right part is the schematic diagram of the artificial neural networks based on the coupling of five MoS_2 -based memristive devices. A, B, C and D represent four presynaptic terminal electrodes; G represents a postsynaptic terminal electrode. Panel **d** is adapted from ref. 11, Springer Nature Limited.

hetero-phase junction^{11,41}. Such a semiconducting-metallic (2H-1T/1T') hetero-phase junction opens up new opportunities in TMD electronics^{11,41}. A notable example is a superior MoS_2 transistor with low-resistance contacts, which was created using the MoS_2 hetero-phase junction produced by local (spatially controlled) Li^+ intercalation¹¹ (Fig. 3d). The well-patterned metallic 1T- MoS_2 region serves as the contact of these transistors, providing a contact resistance (200–300 $\Omega \mu\text{m}$) lower than that of frequently used metal (such as Au) contacts (0.7–10 k $\Omega \mu\text{m}$). Such a transistor has a boosted device performance, including high drive currents, large on/off ratios, high electron mobility and low sub-threshold swing values¹¹ – a performance index that measures the mutual conversion rate between the on/off states of a transistor. In addition, the produced MoS_2 semiconducting-metallic (2H-1T/1T') hetero-phase junction has also been applied in the fabrication of a flexible, ultrafast Schottky diode with a cut-off frequency of 10 GHz without external bias⁴¹ (Fig. 3e) – the Schottky diode (also known as Schottky barrier diode or hot-carrier diode) is a semiconductor diode formed via a semiconductor-metal junction. Integrating a flexible Wi-Fi band antenna into such a diode, a special kind of fully flexible and integrated, battery-free antenna (called rectenna or rectifying antenna) was constructed, which can wirelessly harvest electromagnetic radiation in the Wi-Fi band (2.4 GHz and 5.9 GHz)⁴¹.

Reversible intercalation of alkali metal ions also leads to reversible phase transitions of 2D MoS_2 – this endows the material intriguing opportunities for the application as memristive devices¹³ (Fig. 3f); memristive devices are electrical resistance switches (two-terminal 'memory resistors') that have memory functions and can retain an internal resistance state according to the history of applied voltage and current⁸⁴. By coupling several Li_xMoS_2 -based memristive devices into a network sharing an electrode, the synaptic interactions in artificial neural networks can be emulated of great interest in neuromorphic computing¹³.

Beyond the conventional 2H-1T/1T' phase transition in TMDs, a study has also demonstrated an unconventional-phase transition in WS_2 – from a semimetallic 1T' phase to a semiconducting 1T'_d phase (a distorted octahedral phase) – induced by proton intercalation⁷⁸. Such a phase transition is also reversible, which opens up the possibility of its use in the application of transistors, memory devices and neuromorphic computing.

In addition to MoS_2 and WS_2 , intercalation-induced structural phase transitions are also widely present in other TMDs, such as MoSe_2 (ref. 85), WTe_2 (ref. 86), TiS_2 (ref. 79), TaS_2 (ref. 87) and TaSe_2 (ref. 87).

Intercalation-induced bond reconstructions have also been seen in other 2D vdW materials beyond TMDs, such as BP, MoO_3 and MnO_2 (refs. 30,77,80). For example, intercalation of Li^+ in BP is predicted to break the P–P bond, resulting in a local structural transition from an orthorhombic lattice to an assembly of parallel nanoribbons with rhombohedra-like symmetry⁷⁷. These parallel, narrow nanoribbons often undergo a self-healing process during the Li de-intercalation, resulting in the formation of blue phosphorene⁷⁷. This blue phosphorene is predicted to form a distinctive crystalline and electronic structure⁸⁸ (characterized by buckled honeycomb lattice and has a wider bandgap of -1.1 eV compared with black phosphorene -0.3 eV), opening new opportunities in electronic and optoelectronic applications.

In brief, intercalation-induced charge transfer can lead to in-plane bond reconstruction, leading to structural phase transitions of the 2D materials; this is especially the case for TMDs. Following a phase change, the materials often exhibit entirely different properties⁸³, generating the potential for diverse applications, from electronic devices¹¹ to catalysis⁸⁹, to batteries⁷⁹ and to supercapacitors⁹⁰. Impressively, spatially controlled intercalation and reversible intercalation can induce spatially controlled phase transitions^{11,41} and reversible phase transitions¹³, respectively, providing intriguing opportunities for their application in modern devices such as lower contact resistance transistors¹¹, ultrafast Schottky diodes⁴¹ and memristive devices¹³.

Beyond these opportunities, structural phase transitions may also lead to drawbacks. For instance, the 2H-to-1T phase transition may remove the original semiconducting properties of 2D TMDs, destroying their versatile use in applications ranging from semiconductor devices to photocatalysis. Decreasing the amount of electrons inserted into a system by using large intercalation species (such as tetraheptylammonium ions, THA^+) is a plausible method of preventing phase transitions during the intercalation process⁴⁰.

Shifts of Fermi level and changes in electronic band structures

Intercalation-induced electron injection often results in the increase of free electron density in 2D materials, thereby elevating the Fermi level of 2D materials. For example, after Cu intercalation, the Fermi level of Bi_2Se_3 is raised to the conduction band – known as a Burstein–Moss shift of the bandgap, leading to an increase of the effective bandgap⁹¹ (Fig. 4a). In such band structures, electron transitions from the valence band to the bottom level of the conduction band are prohibited. Instead, electron transitions occur between the valence band and the

Fig. 4 | How intercalation shifts Fermi levels, alters electronic band structures and tunes spin–orbit effects and lattice parameters. **a**, The top left part is a schematic illustration of Cu intercalation in Bi_2Se_3 . The top right part is the band diagram of Cu-intercalated Bi_2Se_3 , showing the Fermi level of Bi_2Se_3 raised to the conduction band – known as Burstein–Moss shift of the bandgap – upon intercalation. The bottom part is the calculated band structure of Bi_2Se_3 before and after Cu intercalation. The black dotted line indicates the position of Fermi levels. **b**, Optical transmission images of Bi_2Se_3 before (left part) and after Cu intercalation (right part), showing an increase in the optical transparency. **c**, Electronic structure of molybdenum disulfide (MoS_2) before and after lithium-ion (Li^+) intercalation, showing an overlap of the conduction band and the valence band of MoS_2 after Li^+ intercalation. **d**, A schematic illustration of calcium (Ca) intercalation in bilayer graphene (the top part) and the angle-resolved photoemission spectroscopic

(ARPES) images of bilayer graphene before and after Ca intercalation (the bottom part). The ARPES image shows a side-by-side comparison of the experimental valence band structure of bilayer graphene before and after Ca intercalation. Downward shift of the $\text{C}2\text{p}$ π and σ bands caused by Ca intercalation is vividly seen (as indicated by the white arrows), which results in the movement of the Fermi-level (E_F) crossing point of the π^* band away from the K point. **e**, A schematic illustration of the tantalum (Ta) intercalation in tantalum disulfide (TaS_2) and the charge density difference in TaS_2 -Ta- TaS_2 , highlighting the electron transfer from the intercalated Ta atom to the Ta in the TaS_2 layer. **f**, Intercalation of Li^+ in Fe_3GeTe_2 bilayer and an illustration showing the spin redistribution mechanism of the Fe- $3d$ bands. Panels **a** and **b** are adapted from ref. 91, Springer Nature Limited. Panel **d** is adapted with permission from ref. 97, National Academy of Sciences. Panel **e** is adapted from ref. 8, Springer Nature Limited.

first unoccupied level above the Fermi level. The degree of the Fermi level shift is related to the carrier density, which normally increases linearly with the concentration of foreign species. For instance, when the injected carrier density reaches about $6 \times 10^{14} \text{ cm}^{-2}$ per layer for LiC_6 , the Fermi level shifts up about 1.5 eV (ref. 92). This up-shift of the Fermi level often leads to the suppression of interband optical transitions^{91,93}, thereby decreasing the optical conductivity and enhancing optical transparency^{91,93–95}. The substantial enhancement of optical transparencies has been demonstrated in conductors (for instance, Li-intercalated 2D graphite⁹³), semiconductors (for example, Li-intercalated MoS_2 (refs. 94,95)) and topological insulators (such as Cu-intercalated Bi_2Se_3 (ref. 91)) (Fig. 4b). This opens up new opportunities for applications in transparent optoelectronic devices. Intercalation-induced electron injection can also markedly change the electronic band structure of 2D materials, thus tuning the electronic properties^{94,96}. An overlap of the conduction and valence bands is found in Li-intercalated 2D TMDs⁹⁴ (Fig. 4c), in which the Fermi level lies in an incompletely filled band. Such a band structure results in a metallic behaviour of the intercalated 2D TMDs with high conductivity. Both the increase in optical transparency and the increase in conductivity make intercalated 2D materials a potential candidate for touchscreen applications.

Additionally, the rise of the Fermi level, the enhancement of the density of states at the Fermi level and the changes of electronic band structures may induce strongly correlated phenomena in 2D materials, such as superconductivity^{97–102}. For example, an exotic superconducting state appears in Ca-intercalated bilayer graphene⁹⁷. Angle-resolved photoemission spectroscopy observed electron doping behaviour from an intercalant (Ca) in bilayer graphene, by a side-by-side comparison of the graphene valence-band structure before and after intercalation (Fig. 4d). Such behaviour induced a free electron-like interlayer band at the Brillouin-zone centre and a large π^* Fermi surface at the zone boundary, which is believed to be the reason for its superconductivity⁹⁷.

In short, intercalation-induced electron injection can result in a shift of the Fermi level and changes in the electronic band structure of 2D materials. These changes can be used to tune various properties, including decreasing optical conductivity and increasing of the optical transparency^{91,93–95}, enhancing electrical conductivity^{94,96}, generating strongly correlated phenomena (such as superconductivity^{97–102}) as well as changing the thermodynamic stability of 2D materials¹⁰³.

Tuning spin–orbit effects and lattice parameters

Intercalation-induced charge transfer and redistribution can tune the spin–orbit effects and lattice parameters of 2D materials, thus

affecting their magnetic properties or triggering magnetic phase transitions^{8,62,104–106}. For instance, self-intercalation of Ta atoms can trigger an electron transfer from an intercalated Ta atom – which is octahedrally coordinated – to the host Ta atom in the TaS_2 layer, which is typically prismatic coordinated⁸ (Fig. 4e). Such an electron transfer and redistribution endow TaS_2 bilayers with a magnetic ground state, whose perfect counterparts (TaS_2 bilayer without intercalation) possess a non-magnetic ground state. The intercalated Ta atoms introduce additional spin-split bands across the Fermi level (see Supplementary Text 1 for details), which is the reason the magnetic ground state is developed. In such a TaS_2 -Ta- TaS_2 superstructure, the magnetic moments are localized on the d orbitals of the intercalated Ta atom.

A first-principles computational study predicted an electron transfer from intercalated Li^+ to interfacial Te sublayers in ferromagnetic vdW Fe_3GeTe_2 bilayer¹⁰⁵ (Fig. 4f). Such electron transfers lift the Fermi level of this metallic system (parts 1 and 2 in Fig. 4f), whereas the Fe sites are not injected with electrons to fill their unoccupied $3d$ states above the original Fermi level. To ‘catch up’ with the up-shifted Fermi level, the spin-down channel (the minority spin channel) of the Fe- $3d$ bands needs to provide electrons to the spin-up channel (the majority spin channel) and then the states move upward (part 3 in Fig. 4f). Finally, the exchange splitting between the two spin channels is increased (part 4 in Fig. 4f). A boosted spin exchange such as this is beneficial for enhancing the interlayer ferromagnetic coupling, favouring stronger ferromagnetism. Notably, over-intercalation may induce excessive electron transfer, resulting in the majority of the spin channel being filled up, which reduces the interlayer ferromagnetic coupling.

Intercalation-induced charge transfer can also trigger magnetic phase transitions in magnetic materials. The transitions of NiPS_3 between its antiferromagnetic and ferrimagnetic phase by tetraheptylammonium bromide intercalation have been observed¹⁰⁶. Such magnetic phase transitions are related to intercalation-induced electron injections and determined by the amount of electrons injected. A low injection level (0.2–0.5 electrons per cell) leads to a ferrimagnetism to antiferromagnetism transition. A high injection level (≥ 0.6 electrons per cell) results in an antiferromagnetism to ferrimagnetism transition. These intercalation-created emerging 2D magnetic materials hold promise for miniaturized and ultralow-power electronic devices that exploit spin manipulation.

In situ studies of intercalation

The nature of intercalated 2D materials can be probed ex situ (Box 3), whereas insights regarding intercalation behaviour and dynamics require in situ studies. Here, we specifically focus on electrochemical

Box 3

Ex situ characterizations of intercalation in 2D materials

Ex situ characterizations of intercalation are in full swing, which can provide comprehensive detection of the tuned natures of intercalated 2D materials.

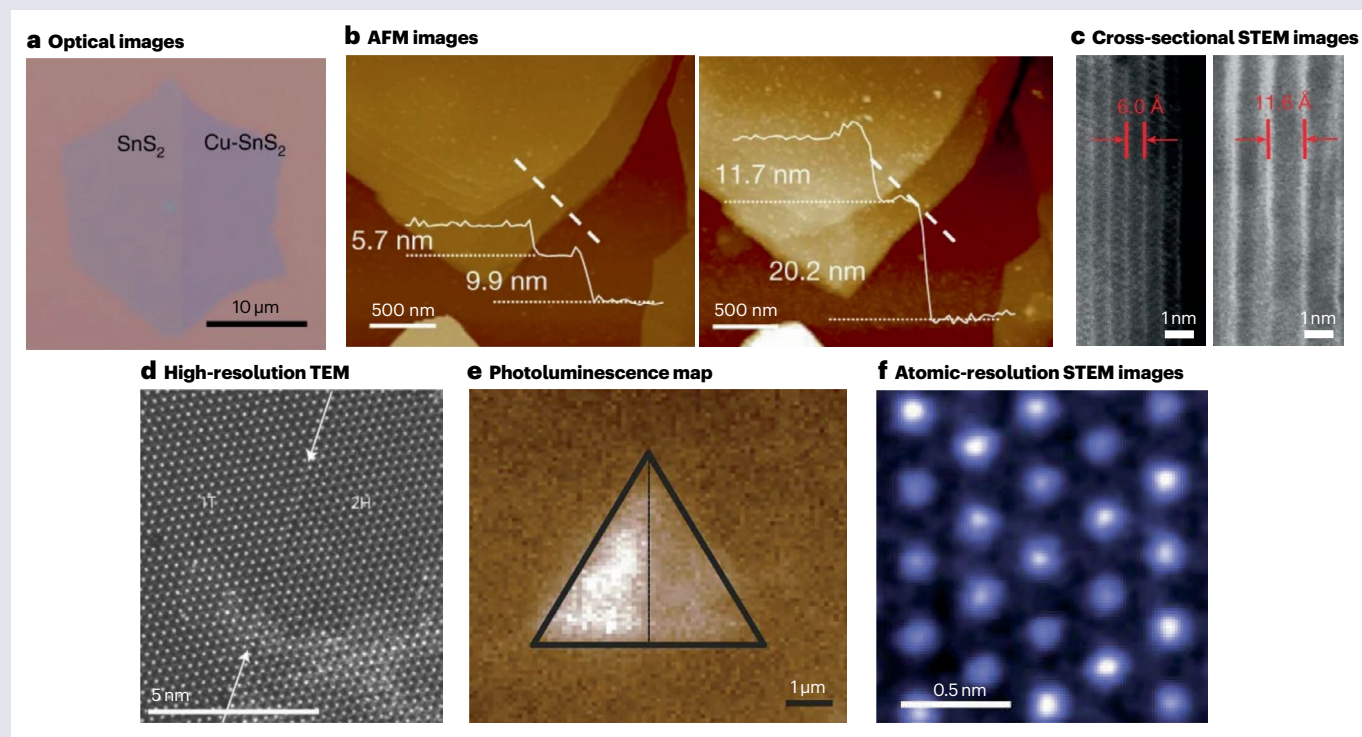
Intercalation-tuned optical properties of 2D materials can be directly visualized via an optical microscope^{9,30,52}. Differences in optical contrast (colour) before and after intercalation can be clearly shown in the optical images (see the figure, part **a**, in which an optical image of an SnS₂ sheet — the left half is intercalated and the right half is unintercalated — is presented). Photoluminescence^{15,29}, optical transmission/reflection spectra⁹¹ and circular dichroism spectroscopy¹⁷ are also available to reflect the changes in the optical properties of intercalated 2D materials. The changes in optical properties of 2D materials are often related to their electronic structures, which can be detected via angle-resolved photoemission spectroscopy^{97,141,186} (see the bottom part of Fig. 4d) and verified or predicted via density functional theory calculations^{15,29,91} (see the right part of Fig. 4a).

Atomic force microscope (AFM) offers a means to probe the intercalation-triggered c-axis lattice expansion^{15,17,29}. An increase in the interlayer distance of 2D materials caused by intercalation can be evidenced in such AFM images (see the figure, part **b**, which shows that after S- α -methylbenzylamine intercalation, the thickness of the TaS₂ nanosheet increases from 9.9 (5.7) nm to 20.2 (11.7) nm). Cross-sectional transmission electron microscopy (TEM)^{15,29} (Fig. 2c) and scanning transmission electron

microscopy (STEM)¹⁷ (see the figure, part **c**, illustrating that after S- α -methylbenzylamine intercalation, the interlayer distance of TaS₂ increases from 6.0 Å to 11.6 Å) are also commonly used to test the increased interlayer spacing. The interlayer distance of intercalated 2D materials can also be obtained by the calculation based on the X-ray diffraction data^{15,17,40}.

Intercalation-induced phase transitions are often confirmed via X-ray photoelectron spectroscopy and Raman spectroscopy based on feature fingerprint peaks^{13,24}. Such phase transitions can also be directly observed through high-resolution transmission electron microscopy (HRTEM)¹¹. The differences in atomic arrangement of 2D materials with different phases can be clearly distinguished in such HRTEM images (see the figure, part **d**, in which a HRTEM image of an MoS₂ sheet is shown — the left half is 1T phase and the right half is 2H phase). Photoluminescence map (see the figure, part **e**, in which an image of a triangular MoS₂ sheet is shown — the left region is the 2H phase and the right region is the 1T phase in which photoluminescence is considerably quenched) and electrostatic force microscopy (see the left part of Fig. 3d) are also feasible tools to image the intercalation-induced phase transitions¹¹.

Additionally, intercalation in 2D materials can also be probed by some other ex situ characterization technologies¹⁸⁷. For example, the amount of the intercalated foreign species can be detected via nuclear magnetic resonance (NMR)⁵³. The elemental composition and distribution of intercalated 2D materials can be examined by



(continued from previous page)

energy-dispersive X-ray spectroscopy¹⁵. Atomic-resolution STEM opens the door for the imaging of intercalated atoms⁸ (see the figure, part **f**, which shows a STEM-annular dark field image of a Ta-intercalated TaS₂ sheet). In this image, the periodically arranged bright spots are attributed to the intercalated Ta atoms.

Panel **a** is reprinted from ref. 9, Springer Nature Limited. Panels **b** and **c** are adapted from ref. 17, Springer Nature Limited. Panels **d** and **e** are reprinted from ref. 11, Springer Nature Limited. Panel **f** is reprinted from ref. 8, Springer Nature Limited.

intercalation of 2D materials. Both chemical intercalation and electrochemical intercalation can drive guest species into the vdW gap of 2D materials, but the latter provides better control of the dynamic intercalation process, such as precise and reversible control of the intercalant concentration. This method is also operated at room temperature, which is beneficial for in situ characterization. Additionally, the charge–discharge mechanism of rechargeable batteries also involves electrochemical intercalation and de-intercalation^{107,108}.

Design of on-chip platforms for in situ studies

To perform in situ studies of the intercalation process in 2D materials, an on-chip electrochemical platform must be built. Such a platform can not only provide a complete circuit to achieve the electrochemical intercalation but also allow the beam probe to reach the 2D material of interest in situ. The platform can be divided into three regions: enclosed (the electrolyte is encapsulated in an enclosed micro–nano space, as seen in Fig. 5a,c), semi-enclosed (the electrolyte is placed in an open-top reservoir, see Fig. 5b) and open (the electrolyte sits directly on the substrate and is fully exposed to the environment, see Fig. 5d,e), in which the platform design depends on the electrolyte type and the characterization technique. A liquid electrolyte requires an enclosed platform to prevent leaks^{35,69,93,94} (Fig. 5a). The electrodes and electrolytes are normally sealed between the chip (SiO₂/Si) and a cover glass using epoxy^{69,94}, polydimethylsiloxane⁹³ or a hot melt sealing film³⁵. This cover is also a window for the beam probe (such as laser) and the glass should therefore be transparent to minimize signal loss of the testing beam. A semi-enclosed platform can also be used for liquid electrolyte systems^{15,61,78} (Fig. 5b), in which such platforms have an open reservoir built into it by patterned polydimethylsiloxane. The targeted 2D material – as the working electrode – is usually located on the chip and in the centre of the reservoir, whereas the counter electrode and reference electrode can be introduced from the open top, forming a complete circuit.

The enclosed and semi-enclosed platforms are normally used for in situ optical microscopy and Raman spectroscopy studies. When in situ TEM imaging of the liquid electrolyte system is required, a carefully designed electrochemical platform is required^{109,110} (Fig. 5c). The electrode and the electrolyte are normally encapsulated between two SiN_x windows with the side edges sealed with indium or an O-ring. This platform allows electron beams to pass through the upper SiN_x window to reach the target 2D material, followed by passing through the 2D materials and exiting from the lower SiN_x window. Also, for in situ atomic force microscopic (AFM) studies, the aforementioned enclosed and semi-enclosed platforms are not applicable. AFM is used to study the surface structure and the properties of the sample by detecting the weak atomic interaction forces between the sample surface and the microforce sensing element (the tip). In the contact mode, an AFM needs physical proximity, free movement and contact between the tip and the sample, which means that the platform must have an open surface for in situ testing^{111–114}. Such open platforms can be built

by simply depositing 2D materials on the substrate (such as SiO₂/Si or glass) before adding external circuitry¹¹¹. It should be noted that such an open platform carries the risk of liquid electrolyte leakage.

When a solid-state electrolyte is used, an open platform is often applied for testing^{12,14,36,115,116} (Fig. 5d). In such platforms, the electrodes are patterned on a substrate and directly exposed to the testing beam (such as laser and electron beam). The electrolyte must be patterned and cured (heat curing^{14,116} or ultraviolet curing^{12,36}) around the counter electrode and connected to the working electrode to form a complete circuit. This allows the beam probe access to the 2D materials without obstruction by the electrolyte. The cured electrolytes should be capped by a 200 nm coating of evaporated SiO_x to avoid outgassing and oxidation in air³⁶. The substrate used in this platform is usually an SiO₂/Si plate^{12,14,115,116}. Such platforms have been used with a range of techniques from photoluminescence¹⁴ and Raman spectroscopy¹¹⁶, X-ray diffraction (XRD)¹¹⁵ and electrical transport¹². For in situ TEM testing, SiN_x-covered Si chip with a central hole is often used as a substrate in which the 2D materials are placed, covering the hole and facilitating the electron beam penetration through the probed 2D material³⁶ (Fig. 5e).

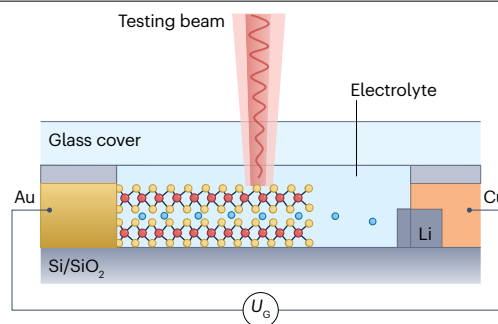
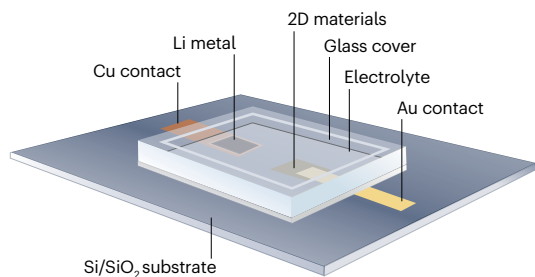
In situ imaging studies

In situ spatially resolved, time-domain imaging techniques (such as in situ optical microscopy, thermal conductance microscopy, TEM and AFM) can visualize the intercalation process. With it, behaviour and dynamics, such as the intercalation pathways, reversibility, uniformity and rates, can be observed or determined.

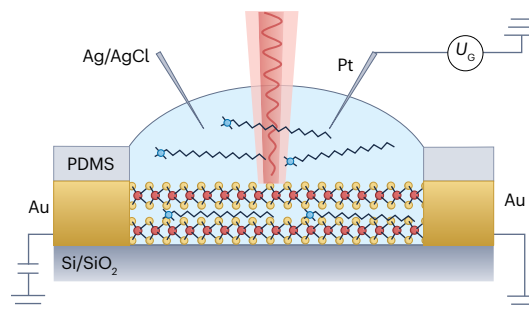
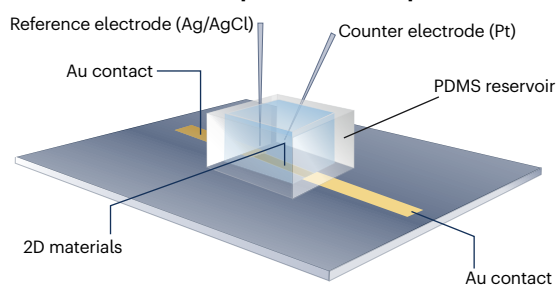
Optical microscopy is a common spatially resolved, time-domain tool for these studies^{35,86,93,94,117}. Intercalation of 2D materials is followed by a change in the optical contrast, and a microscope can detect this. The intercalation behaviour of Li⁺ in 2D MoS₂ was imaged^{35,94,117} and showed a gradual darkening from the edges to the centre, before covering the entire flake⁹⁴ (the top part of Fig. 6a). This clearly indicates that intercalation of foreign species starts from the edge of this kind of 2D material. After a de-intercalation treatment, the colour of the thicker parts of the MoS₂ material had not completely returned to its original yellow shade, but instead had a reddish tint (the bottom part of Fig. 6a). This suggests that thicker MoS₂ is unable to recover fully from lithiation, possibly accompanied by the structural damage. This work provided the first evidence for the dynamics of Li⁺ intercalation in 2D TMDs, demonstrating the associated spatial inhomogeneity and cycling-induced structural defects during the Li⁺ intercalation and de-intercalation process. These results offer a possible explanation for the loss of cyclic capacity of TMD materials in energy storage devices. Additionally, the noted observations proved that intercalation could improve the optical transmission of 2D materials. These findings imply potential applications in optoelectronics and transparent electrodes.

In situ optical microscopy also demonstrated better stability, uniformity and reversibility when intercalation proceeded from the top rather than from the edge when they are sealed³⁵. The ion selectivity

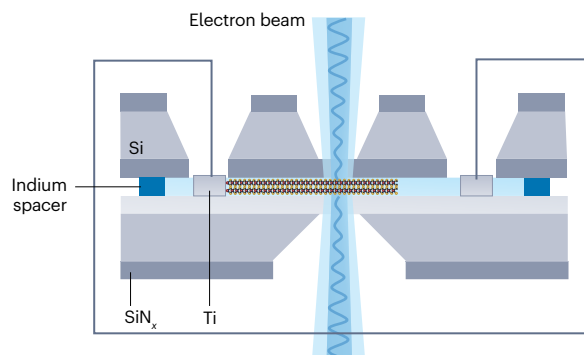
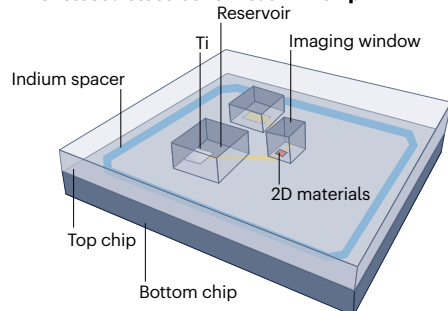
a An enclosed on-chip electrochemical platform



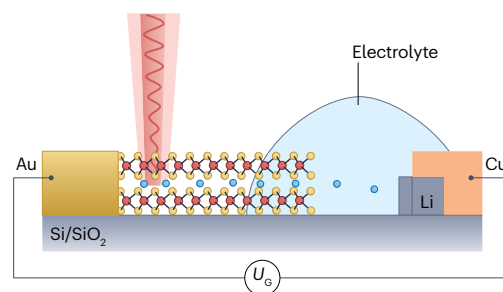
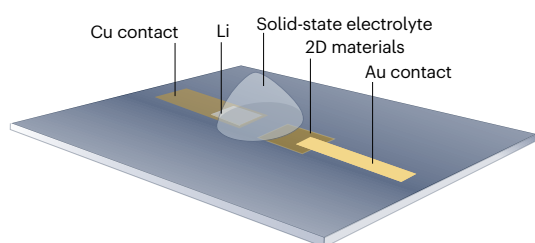
b A semi-enclosed on-chip electrochemical platform



c An enclosed electrochemical TEM chip



d An open on-chip electrochemical platform



e An open on-chip electrochemical platform for TEM testing

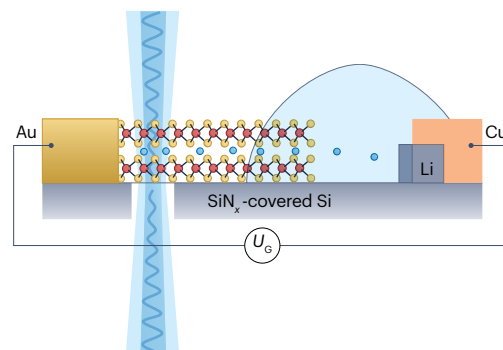
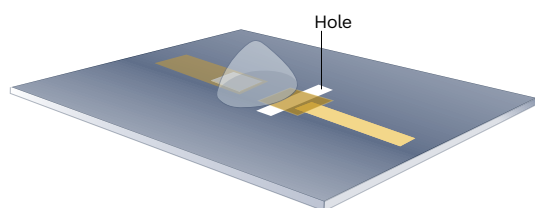


Fig. 5 | Design of on-chip platform for in situ studies of intercalation in 2D materials. **a**, An enclosed on-chip electrochemical platform. The electrodes and electrolytes are encapsulated between the chip (SiO₂/Si) and a cover glass. **b**, A semi-enclosed on-chip electrochemical platform. The electrolyte and the working electrode are placed in the open-top reservoir, whereas the counter electrode and reference electrode are introduced from the open top. **c**, An enclosed electrochemical transmission electron microscopic (TEM) chip.

The electrode and the electrolyte are encapsulated between two SiN_x windows (which allow electron beams to pass through) with the side edges sealed with indium or an O-ring. **d**, An open on-chip electrochemical platform. The solid-state electrodes are patterned on the substrate and directly exposed to the testing beam. **e**, An open on-chip electrochemical platform with a hole for TEM testing. The solid-state electrodes are patterned on an SiN_x-covered Si chip with a central hole and directly exposed to the electron beam. PDMS, polydimethylsiloxane.

behaviour of this intercalation method has also been proven to allow small Li⁺ and sodium ions (Na⁺) into the interlayer spacing, while rejecting larger ions such as potassium ions (K⁺)³⁵. These results lay the foundation for the application of intercalation in developing functional devices with high tunability and ion selectivity. They also provide guidance for developing 2D-material-based films for selective ionic sieving and desalinating of salt water.

In situ thermal conductance microscopy provides spatial imaging of the thermo-reflectance of 2D materials⁶⁹. Using this tool, Li⁺ were further confirmed to preferentially intercalate from unobstructed edges of MoS₂ (ref. 69) (Fig. 6b). This technique also proves that intercalation of Li⁺ can reduce cross-plane thermal transport in 2D MoS₂ (ref. 69). With first-principles calculations, the intrinsic mechanism of thermal transport modulation was shown to be through phonon scattering, *c*-axis strain and crystal-structure stacking disorder induced by the lithium intercalation⁶⁹. These results open the door for developing electrochemically driven nanoscale thermal regulators.

In situ TEM provides a visual of morphology changes^{110,118}, as well as the opportunity to probe the dynamics of phase transitions in 2D materials during intercalation processes owing to its high spatial resolution (quasi-atomic level). The 1T/1T' phase nucleation and 2H-1T/1T' phase boundary propagation of MoS₂ induced by Li⁺ or Na⁺ intercalation have been probed thoroughly by in situ TEM^{119,120}. The dynamic evolutions of the chemical compositions have been tracked by combining in situ TEM with in situ selected area electron diffraction and electron energy loss spectroscopy mapping^{119,121,122}. Upon decomposition of MoS₂ caused by excessive Li⁺ intercalation, an amorphous Li₃S matrix and Mo atoms form¹¹⁹, highlighting the dangers of over-intercalation. The complex multistep intercalation and reaction in 2D materials can also be traced by these in situ technologies^{121,123}. For example, the full scenario of the lithiation process of the 2D SnS₂ has been observed¹²¹; the whole intercalation process proceeds the following four steps: the intercalation reaction (SnS₂ + *x*Li⁺ + *x*e⁻ → Li_{*x*}SnS₂), disordering reaction (Li_{*x*}SnS₂ → Li_{*y*}SnS₂), conversion reaction (Li_{*y*}SnS₂ → Li₂S + Sn) and the alloying reaction (Sn + *x*Li + *x*e⁻ → Li_{*x*}Sn)¹²¹.

However, conventional in situ TEM is unsuitable for characterizing the intercalation of light elements (especially Li) mainly owing to the low scattering cross-section of light elements not being conducive to receiving electrons, and that light elements are highly susceptible to damage caused by the impacting electrons³⁶. Low-voltage in situ TEM provides the solution as its electron acceleration voltage can be kept below the threshold for damaging light elements and the 2D materials³⁶. With low-voltage in situ TEM at sub-Ångstrom resolution, real-time observations of reversible intercalation and the alignment of Li⁺ in a graphene double layer were achieved³⁶. These observations demonstrated that Li⁺ form very dense multilayers and closely packed, ordered structures in the middle of double-layer graphene sheets (Fig. 6c) – leading to high-capacity lithium storage. This study demonstrates the significant advantages of 2D materials in improving the capacity of lithium batteries.

The thickness and surface morphological evolution of 2D materials caused by intercalation can also be visualized through in situ AFM^{111–114}. The appearance and retention of wrinkling of 2D TMDs during Li⁺ and Na⁺ intercalation and de-intercalation processes have been identified by this tool^{111,112,114}. These results testify the inherent flexibility of 2D TMDs and the failure mechanism of TMD-based lithium-ion or sodium-ion batteries.

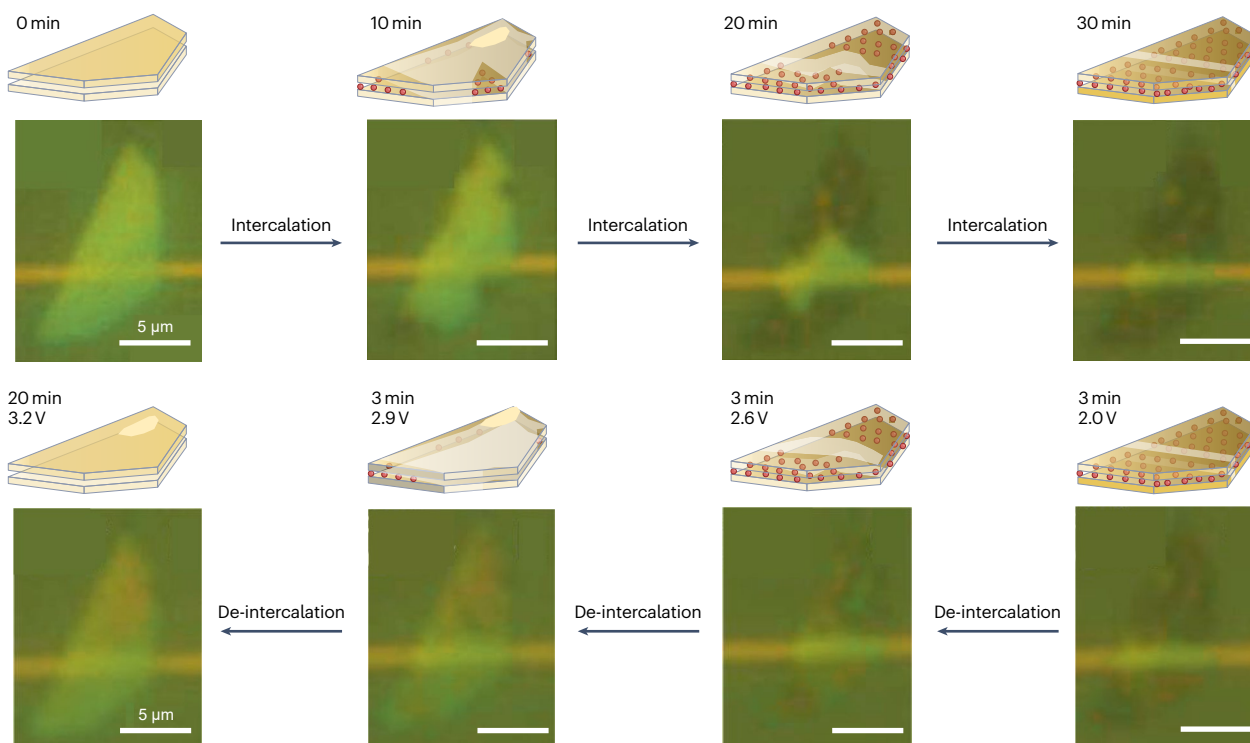
Alternate in situ studies

In situ spectroscopic techniques record the effects of intercalation through the fingerprint region of a spectrum of targeted 2D materials^{14,15,115,124,125}. The peak position, strength and shifts can reflect the basic properties of 2D materials such as the number layers, its phase and lattice stresses.

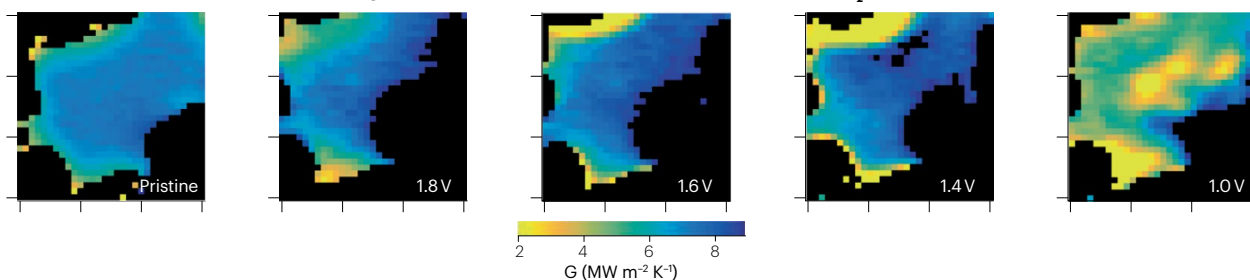
Raman spectroscopy is often used to detect the structural phase transitions of 2D materials during the intercalation process. For example, 2H-MoS₂ has two Raman-active modes in the fingerprint region, A_{1g} and E_{2g}¹, corresponding to the out-of-plane and in-plane vibrations – located at 380 cm⁻¹ and 406 cm⁻¹, respectively^{40,126}. Following a phase transition, 1T-MoS₂ exhibits three weak but distinct new peaks: J₁ (150 cm⁻¹), J₂ (225 cm⁻¹) and J₃ (327 cm⁻¹)^{13,24}. Among others, the phase transitions of 2H-to-1T/1T' in 2D MoS₂ (refs. 35,94,127), 1T'-to-1T'_d in WS₂ (ref. 78) and T_d-to-T'_d in WTe₂ (ref. 86) have also been studied with Raman spectroscopy. In addition, this vibrational technique has been used to understand the Li⁺ intercalation process in graphene by studying the shifts and sharpening of its G-band and 2D-band at -1,600 cm⁻¹ and -2,700 cm⁻¹, respectively^{116,128,129}. Intercalation-induced local strain and displacement of the graphene lattice were detected in these studies^{116,128,129}.

Beyond Raman, in situ XRD^{79,115} and photoluminescence¹⁴ are also the potential in situ probes, giving real-time information of lattice parameters, crystal structures, phase transitions, lattice strain, compositions and optical properties during intercalation. Although these techniques (particularly in situ XRD) are of great importance and widely used in understanding of the intercalation process of layered materials (especially for the layered electrode material in electrochemical energy storage devices^{38,130}, see Supplementary Text 2 for details), their power has not yet been fully utilized in the study of intercalation in atomically thin 2D materials. The technical reason lies in the low detection sensitivity of XRD owing to its need for relatively thick and large amounts of sample, which contradicts the nature of the discussed 2D materials (often only a few atomic layers in thicknesses). Although the sensitivity of XRD is lower than that of Raman spectroscopy, its resolution is typically higher, which can determine the crystal structure and phase composition more accurately. As such, if the detection sensitivity of XRD can be improved, deeper insights regarding intercalation in atomically thin 2D materials might be gained. Now, there is a rising technique – grazing incident XRD – which allows X-rays to skim the sample surface, as the test ray is almost parallel to the sample plane. Such a technology has high sensitivity for the detection of 2D material

a In situ optical microscopic observations of lithium-ion intercalation and de-intercalation in 2D MoS₂ sheet



b In situ thermal conductance microscopic observations of lithium-ion intercalation in 2D MoS₂ sheet



c In situ TEM observations of lithium-ion intercalation in double-layer graphene sheet

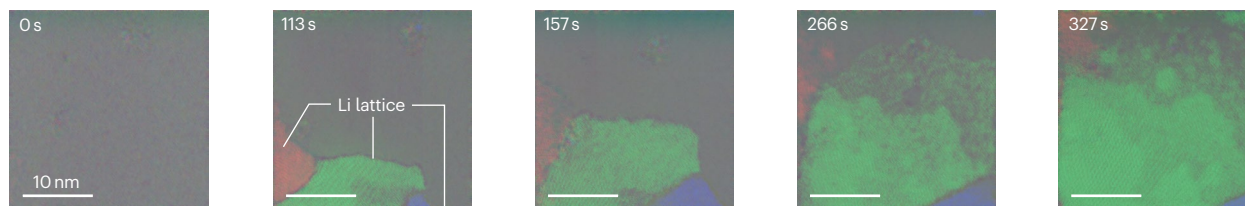


Fig. 6 | In situ studies of intercalation in 2D materials. **a**, Illustrations and in situ optical microscopic observation of lithium-ion (Li⁺) intercalation (top panels) and de-intercalation (bottom panels) in 2D MoS₂ sheets. The colour of the MoS₂ flake gradually darkens from the edges to the centre during intercalation and gradually recovers during de-intercalation. The top first image was taken at a voltage of 2.1 V versus Li/Li⁺, leading to no intercalation. The second to fourth images were taken at a voltage of 1.1 V versus Li/Li⁺, during which intercalation occurs. The bottom panels, in the order from right to left, are images taken at 3-min intervals increasing voltages. **b**, In situ thermal conductance microscopic

observation of Li⁺ intercalation in 2D MoS₂ sheet, exhibiting cross-plane thermal transport of the 2D MoS₂ sheet, which gradually decreases from the edge to the centre. **c**, In situ transmission electron microscopic (TEM) observation of Li⁺ intercalation in double-layer graphene sheets, demonstrating that Li⁺ forms multilayer ultra-dense and closely packed ordered structure in the middle of double-layer graphene sheets. Red, green and blue indicate intercalated Li⁺ crystalline grains of different orientations. Part **a** adapted with permission from ref. 94, ACS. Panel **b** reprinted from ref. 69 under a Creative Commons licence CC BY 4.0 Panel **c** adapted from ref. 36, Springer Nature Limited.

films^{131,132} and could be a powerful tool in the near future to advance intercalation detection in 2D materials¹¹⁵.

Looking ahead at in situ studies

In situ studies of intercalation in 2D materials are ongoing, but it is not yet in full swing. Certain state-of-the-art techniques are not fully utilized, but they have enormous potential for furthering our understanding of the chemistry and physics behind intercalation mechanisms.

For example, in situ transmission X-ray microscopy¹³³, scanning transmission X-ray microscopy^{134,135}, Bragg coherent X-ray diffraction imaging¹³⁶ or X-ray phase contrast holotomography¹³⁷ may open the door for visualizing the structural evolution in 3D space of 2D materials during intercalation (both horizontal and vertical spaces). These techniques can compensate for the shortcomings of TEM and AFM, which can only detect 2D space. This will achieve simultaneous detection of transverse and longitudinal diffusion and the distribution of intercalants in 2D materials, which will benefit our understanding considerably.

Time-resolved photoemission electron microscopy, which combines femtosecond laser pump-probe techniques with spectroscopic photoemission electron microscopy, may offer an opportunity for imaging electron motion in 2D materials during intercalation with high spatial and temporal resolution¹³⁸. This will provide unprecedented insights into the behaviour of electrons driven by electric fields or photo-excitation in semiconductor devices (such as transistors and diodes) based on intercalated 2D materials.

Time-resolved and angle-resolved photoemission spectroscopy, enabling time, energy and momentum resolution^{139–141}, may provide quantitative and direct observational access of the Fermi level shift and electronic band structure changes of 2D materials during intercalation^{142,143}. As such, intercalation can be used to quantitatively tune the Fermi level and electronic band structure of 2D materials.

In situ X-ray absorption spectroscopy can detect real-time changes in the structures of 2D materials^{124,144,145}, such as the bond geometry (bond type, coordination number and bond length), paving the way for understanding in-plane bond reconstruction induced by intercalation.

Outlook

When intercalation occurs, a plethora of opportunities appear in the form of property tuning of 2D materials, but intercalation in 2D materials is still in their infancy. Plenty of interesting science awaits to be conducted. Unclear prospects, such as mass production, need to be gradually addressed.

The library of 2D materials is growing continuously with more than 2,000 2D materials having been discovered so far¹⁴⁶, and among them only the famous cases – graphene, MoS₂ and BP – are used for exploring the properties of intercalated materials. As almost every 2D material possesses unusual properties⁵, their intercalation compounds may also have peculiar natures, and there is considerable room for intercalation in diverse 2D materials (such as 2D vdW metal oxide, hexagonal boron nitride and atomically thin MXenes) as well as their vdW heterostructures¹⁴, their twisted structures with Moiré patterns⁴⁷ and their rolled-up 1D system^{147,148}, to create artificial superlattices with exotic physical and interesting chemical properties with desired functionalities.

Various intercalation guest species are continuously enriched, from metal atoms, to diverse ions and to organic molecules^{8,15}. As each species has unique attributes, their insertion may also create various artificial superlattices with exotic functions. For instance, chiral guest molecules can create chiral-induced spin selectivity in 2D TaS₂ and TiS₂, opening up for its application in spintronic devices without external

magnetic fields¹⁷. Therefore, continuously enriching the intercalation species (such as paramagnetic ions¹⁴⁹ – for example, FeCl₄⁻; organic molecules¹⁵⁰ – for instance, small metal-free organic molecules, organometallic coordination complexes and polymers; plasma²⁹ – such as oxygen plasma; even small molecules with biological activity) to create more 2D artificial superlattices with unique functions is a major task for future intercalation studies.

When inserting different species into 2D crystals, the created artificial superlattice may exhibit interesting chemistry and physics. For example, co-intercalation of tetrabutylammonium molecules and metal ions (such as Co²⁺, In³⁺, Pd²⁺ and Fe³⁺) in TaS₂ creates a superlattice with both superconductivity and ferromagnetism⁶². More bifunctional or multifunctional superlattices are expected to become available in the future; for instance, by co-intercalating catalytically active species (such as monoatomic metals¹⁵¹; Pt, Ni and Rh) and magnetically responsive species to create materials, which have catalytic function and are easy to recover with magnetic separation.

Challenges still exist in this area of research. The difficulty lies in how to choose the appropriate intercalation method and condition to achieve intercalation or co-intercalation. This often requires considerable experimentation to select appropriate synthetic variables. Challenges also exist in how to screen well-matched hosts (2D materials) and guests (intercalants) to ensure high stability and required functionality of the created artificial superlattice. The traditional experimental approach to solving these difficulties and challenges is usually time-consuming and labour-intensive. High-throughput computational screening and machine learning may provide a fast track for these explorations⁵⁸. Through it, the intercalation process and effects and the nature of the crafted artificial superlattices can be simulated and predicted, guiding researchers to create more 2D artificial superlattices as needed.

Normally, intercalation in 2D materials is driven by a gradient in concentrations or potentials, and temperature is a way of assisting the process. Are there other ways to achieve intercalation or aid the process, such as using magnetic fields, pressure, microwaves or a combination? This is worth exploring, which is conducive for promoting the emergence of new intercalation methods.

Horizontally spatial-controlled intercalation is striking, and the in-plane heterostructures or hetero-phase structures it creates open up new opportunities in future optoelectronics^{9,11,30,41}. The controllability of longitudinal spatial intercalation has not been achieved. This is difficult but carries enormous potential as the created longitudinal heterostructures with vertical anisotropy will bring a range of possible applications (such as tunnelling transistors, barristors and flexible electronics, resonant tunnelling diodes and light-emitting diodes), just like the currently popular atomic level LEGO^{5,18,152} – representing stacked material, vertically assembled in a chosen sequence, as in building with Lego bricks, in which the blocks are defined with one-atomic-plane precision. For example, the construction of metallic phase 1T-MoS₂ (as a channel material) and semiconducting phase 2H-MoS₂ (as a light-sensitive material, in which photo-charges are generated via light illumination) longitudinal heterostructures may allow the creation of simple and efficient phototransistors. Such 1T/2H MoS₂ longitudinal heterostructures are expected to be formed through vertically controllable Li⁺ intercalation. The intercalated part induces 2H-to-1T phase transitions; the non-intercalated parts do not undergo such phase transitions, retaining their 2H phase. The challenge lies in how to achieve vertical controllability of intercalation in 2D materials. Theoretically, the local wrapping strategy based on lithography^{9,11,30} is a feasible way. However,

implementation is technically challenging, as the thickness of the 2D materials is usually only a few nanometres to tens of nanometres, and at this scale, precise masking and lithography are difficult.

Novel applications with intercalated 2D materials, such as superior MoS₂ transistors with low-resistance contacts¹¹, battery-free rectennas for Wi-Fi band harvesting based on flexible ultrafast MoS₂ Schottky diodes⁴¹ and artificial neural networks based on MoS₂ memristive devices¹³, are on the rise. Most of these exciting devices are still in the proof-of-concept stage, and how to achieve the ‘lab-to-fab’ transition is a challenge. Scaling up research into intercalation methods and reducing intercalation costs should be targeted first. Addressing the challenges in integration and durability related to the practical use of these devices is also important for promoting the lab-to-fab transition.

Intercalation in 2D materials also faces other challenges. For example, intercalation-derived materials are often unstable in air, especially when reactive intercalants (such as alkali and alkali-earth metal ions) are used. Therefore, developing smart strategies for assembling, encapsulating and packing of intercalated 2D materials to improve stability is crucial for future applications. Additionally, there is no clear basis for the selection of intercalation species for achieving purposeful structural modifications of 2D materials. Therefore, establishing a database is urgently needed to summarize previous intercalation studies for organizing and establishing the relationship between intercalated species and structural modifications.

To end, opportunities and challenges coexist in this promising field. We can expect fast progress of intercalation in 2D materials and in situ studies in the coming decades.

Published online: 16 May 2024

References

- Novoselov, K. S. et al. Electric field effect in atomically thin carbon films. *Science* **306**, 666–669 (2004).
- Liu, Y. et al. Promises and prospects of two-dimensional transistors. *Nature* **591**, 43–53 (2021).
- Akinwande, D. et al. Graphene and two-dimensional materials for silicon technology. *Nature* **573**, 507–518 (2019).
- Deng, D. et al. Catalysis with two-dimensional materials and their heterostructures. *Nat. Nanotechnol.* **11**, 218–230 (2016).
- Novoselov, K. S., Mishchenko, A., Carvalho, A. & Castro Neto, A. H. 2D materials and van der Waals heterostructures. *Science* **353**, aac9439 (2016).
- Wu, Y., Li, D., Wu, C.-L., Hwang, H. Y. & Cui, Y. Electrostatic gating and intercalation in 2D materials. *Nat. Rev. Mater.* **8**, 41–53 (2023).
An authoritative review on intercalation and electrostatic gating in 2D materials.
- Koski, K. J. et al. Chemical intercalation of zerovalent metals into 2D layered Bi₂Se₃ nanoribbons. *J. Am. Chem. Soc.* **134**, 13773–13779 (2012).
- Zhao, X. et al. Engineering covalently bonded 2D layered materials by self-intercalation. *Nature* **581**, 171–177 (2020).
A representative work on self-intercalation, presenting the self-intercalation of Ta atoms in 2D TaS₂ crystals, highlighting that self-intercalation is an approach to grow a new class of 2D materials with stoichiometry-dependent or composition-dependent properties.
- Gong, Y. et al. Spatially controlled doping of two-dimensional SnS₂ through intercalation for electronics. *Nat. Nanotechnol.* **13**, 294–299 (2018).
A representative work on spatially controlled intercalation, presenting the spatially controlled intercalation of Cu and/or Co atoms in 2D SnS₂ crystals realized by combining solution-based chemical intercalation with lithography.
- Yu, Y. et al. Gate-tunable phase transitions in thin flakes of 1T-TaS₂. *Nat. Nanotechnol.* **10**, 270–276 (2015).
- Kappera, R. et al. Phase-engineered low-resistance contacts for ultrathin MoS₂ transistors. *Nat. Mater.* **13**, 1128–1134 (2014).
- Kühne, M. et al. Ultrafast lithium diffusion in bilayer graphene. *Nat. Nanotechnol.* **12**, 895–900 (2017).
- Zhu, X., Li, D., Liang, X. & Lu, W. D. Ionic modulation and ionic coupling effects in MoS₂ devices for neuromorphic computing. *Nat. Mater.* **18**, 141–148 (2019).
A representative work on reversible electrochemical intercalation, presenting the reversible intercalation of Li⁺ in 2D MoS₂ crystals, demonstrating that reversible intercalation of alkali metal ions leads to reversible phase transitions of 2D transition metal dichalcogenides.
- Bediako, D. K. et al. Heterointerface effects in the electrointercalation of van der Waals heterostructures. *Nature* **558**, 425–429 (2018).
A representative work on intercalation in 2D van der Waals heterostructures, presenting the electrochemical Li⁺ intercalation in 2D hexagonal boron nitride/MoS₂/graphene/hexagonal boron nitride heterostructures.
- Wang, C. et al. Monolayer atomic crystal molecular superlattices. *Nature* **555**, 231–236 (2018).
A representative work on electrochemical organic ion intercalation, presenting the electrochemical intercalation of cetyl-trimethylammonium ions in 2D black phosphorus crystals, demonstrating that intercalation can trigger c-axis lattice expansion and result in monolayer natures in intercalated 2D materials.
- Wu, Z. et al. Intercalation-driven ferroelectric-to-ferroelastic conversion in a layered hybrid perovskite crystal. *Nat. Commun.* **13**, 3104 (2022).
- Qian, Q. et al. Chiral molecular intercalation superlattices. *Nature* **606**, 902–908 (2022).
A representative work on molecular intercalation, presenting the intercalation of chiral molecules in 2D TaS₂ and TiS₂ crystals, highlighting that chiral molecular intercalation can make the intercalated 2D materials show chiral-induced spin selectivity.
- Geim, A. K. & Grigorieva, I. V. Van der Waals heterostructures. *Nature* **499**, 419–425 (2013).
- Li, Z. et al. Intercalation of atomically thin sheets by the intercalation-based exfoliation of layered materials. *Nat. Synth.* **2**, 101–118 (2023).
An authoritative review on intercalation as a tool for the exfoliation of 2D materials.
- Wan, J. et al. Tuning two-dimensional nanomaterials by intercalation: materials, properties and applications. *Chem. Soc. Rev.* **45**, 6742–6765 (2016).
- Rajapakse, M. et al. Intercalation as a versatile tool for fabrication, property tuning, and phase transitions in 2D materials. *npj 2D Mater. Appl.* **5**, 30 (2021).
- Wang, S. et al. Electrochemical molecular intercalation and exfoliation of solution-processable two-dimensional crystals. *Nat. Protoc.* **18**, 2814–2837 (2023).
- Li, Z. et al. Intercalation strategy in 2D materials for electronics and optoelectronics. *Small Methods* **5**, 2100567 (2021).
- Yang, R. et al. High-yield production of mono- or few-layer transition metal dichalcogenide nanosheets by an electrochemical lithium ion intercalation-based exfoliation method. *Nat. Protoc.* **17**, 358–377 (2022).
A representative work on intercalation as a tool for the exfoliation of 2D materials, presenting the electrochemical intercalation of Li⁺ in bulk materials for the exfoliation production of 2D MoS₂, WS₂, TiS₂, TaS₂, ZrS₂, graphene, hexagonal boron nitride, NbSe₂, WSe₂, Sb₂Se₃ and Bi₂Te₃.
- Chen, H., Ma, H. & Li, C. Host-guest intercalation chemistry in MXenes and its implications for practical applications. *ACS Nano* **15**, 15502–15537 (2021).
- Li, X. et al. MXene chemistry, electrochemistry and energy storage applications. *Nat. Rev. Chem.* **6**, 389–404 (2022).
- Hart, J. L. et al. Control of MXenes’ electronic properties through termination and intercalation. *Nat. Commun.* **10**, 522 (2019).
- Whittingham, M. S. Electrical energy storage and intercalation chemistry. *Science* **192**, 1126–1127 (1976).
- Zhang, L. et al. 2D atomic crystal molecular superlattices by soft plasma intercalation. *Nat. Commun.* **11**, 5960 (2020).
- Wu, Y. et al. Chemical switching of low-loss phonon polaritons in α-MoO₃ by hydrogen intercalation. *Nat. Commun.* **11**, 2646 (2020).
- Jung, N. et al. Optical reflectivity and Raman scattering in few-layer-thick graphene highly doped by K and Rb. *ACS Nano* **5**, 5708–5716 (2011).
- Bointon, T. H. et al. Approaching magnetic ordering in graphene materials by FeCl₃ intercalation. *Nano Lett.* **14**, 1751–1755 (2014).
- Zhou, J. et al. Layered intercalation materials. *Adv. Mater.* **33**, 2004557 (2021).
- Zhu, X. et al. Exfoliation of MoS₂ nanosheets enabled by a redox-potential-matched chemical lithiation reaction. *Nano Lett.* **22**, 2956–2963 (2022).
- Zhang, J. et al. Reversible and selective ion intercalation through the top surface of few-layer MoS₂. *Nat. Commun.* **9**, 5289 (2018).
A representative work on intercalation from the top surface, presenting the Li⁺ and Na⁺ intercalation through the top surface of 2D MoS₂ crystals realized by sealing the edges of MoS₂ with metal or other encapsulating agents.
- Kühne, M. et al. Reversible superdense ordering of lithium between two graphene sheets. *Nature* **564**, 234–239 (2018).
A representative work on in situ transmission electron microscopic observation of intercalation in 2D materials, examining the Li⁺ intercalation and de-intercalation process in double-layer graphene sheet, indicating that Li⁺ tends to form multilayer ultra-dense and closely packed ordered structure in the middle of double-layer graphene sheets.
- Sood, A. et al. Electrochemical ion insertion from the atomic to the device scale. *Nat. Rev. Mater.* **6**, 847–867 (2021).
- Yang, C. et al. Aqueous Li-ion battery enabled by halogen conversion–intercalation chemistry in graphite. *Nature* **569**, 245–250 (2019).
- Cho, J.-H. et al. Controlling the intercalation chemistry to design high-performance dual-salt hybrid rechargeable batteries. *J. Am. Chem. Soc.* **136**, 16116–16119 (2014).
- Lin, Z. et al. Solution-processable 2D semiconductors for high-performance large-area electronics. *Nature* **562**, 254–258 (2018).
A representative work on intercalation as a tool for the exfoliation of 2D materials, presenting the electrochemical intercalation of tetraalkylammonium ions (R₄N⁺) in bulk materials for the exfoliation production of 2D MoS₂, WSe₂, Bi₂Se₃, NbSe₂, In₂Se₃ and Sb₂Te₃.

41. Zhang, X. et al. Two-dimensional MoS₂-enabled flexible rectenna for Wi-Fi-band wireless energy harvesting. *Nature* **566**, 368–372 (2019).
42. Lee, S. W. et al. Anisotropic angstrom-wide conductive channels in black phosphorus by top-down Cu intercalation. *Nano Lett.* **21**, 6336–6342 (2021).
43. Lasek, K. et al. Molecular beam epitaxy of transition metal (Ti-, V-, and Cr-) tellurides: from monolayer ditellurides to multilayer self-intercalation compounds. *ACS Nano* **14**, 8473–8484 (2020).
44. Guzman, R. et al. Collective magnetic behavior in vanadium telluride induced by self-intercalation. *ACS Nano* **17**, 2450–2459 (2023).
45. Pan, S. et al. On-site synthesis and characterizations of atomically-thin nickel tellurides with versatile stoichiometric phases through self-intercalation. *ACS Nano* **16**, 11444–11454 (2022).
46. Gong, Y. et al. Vertical and in-plane heterostructures from WS₂/MoS₂ monolayers. *Nat. Mater.* **13**, 1135–1142 (2014).
47. Wu, Y. et al. Observation of an intermediate state during lithium intercalation of twisted bilayer MoS₂. *Nat. Commun.* **13**, 3008 (2022).
48. Niu, K. et al. Self-intercalated magnetic heterostructures in 2D chromium telluride. *Adv. Funct. Mater.* **33**, 2208528 (2023).
49. Zhang, C. et al. Room-temperature magnetic skyrmions and large topological Hall effect in chromium telluride engineered by self-intercalation. *Adv. Mater.* **35**, 2205967 (2023).
50. Saha, R. et al. Observation of Néel-type skyrmions in acentric self-intercalated Cr_{1+x}Te₂. *Nat. Commun.* **13**, 3965 (2022).
51. Zhang, X. et al. Self-intercalation tunable interlayer exchange coupling in a synthetic van der Waals antiferromagnet. *Adv. Funct. Mater.* **32**, 2202977 (2022).
52. Jiang, H. et al. Single atom catalysts in van der Waals gaps. *Nat. Commun.* **13**, 6863 (2022).
53. Yu, Y. et al. Ultra-thin SnS₂-Pt nanocatalyst for efficient hydrogen evolution reaction. *Nanomaterials* **10**, 2337 (2020).
54. Li, K. et al. Tunable magnetic response in 2D materials via reversible intercalation of paramagnetic ions. *Adv. Electron. Mater.* **5**, 1900040 (2019).
55. Husemović, S. et al. Hard ferromagnetism down to the thinnest limit of iron-intercalated tantalum disulfide. *J. Am. Chem. Soc.* **144**, 12167–12176 (2022).
56. Parvez, K. et al. Exfoliation of graphite into graphene in aqueous solutions of inorganic salts. *J. Am. Chem. Soc.* **136**, 6083–6091 (2014).
57. Liu, N. et al. Large-area atomically thin MoS₂ nanosheets prepared using electrochemical exfoliation. *ACS Nano* **8**, 6902–6910 (2014).
58. Jordan, M. I. & Mitchell, T. M. Machine learning: trends, perspectives, and prospects. *Science* **349**, 255–260 (2015).
59. Gamble, F. R., DiSalvo, F. J., Klemm, R. A. & Geballe, T. H. Superconductivity in layered structure organometallic crystals. *Science* **168**, 568–570 (1970).
60. Pereira, J. M. et al. Percolating superconductivity in air-stable organic-ion intercalated MoS₂. *Adv. Funct. Mater.* **32**, 2208761 (2022).
61. He, Q. et al. In situ probing molecular intercalation in two-dimensional layered semiconductors. *Nano Lett.* **19**, 6819–6826 (2019).
62. Li, Z. et al. Imprinting ferromagnetism and superconductivity in single atomic layers of molecular superlattices. *Adv. Mater.* **32**, 1907645 (2020).
63. Li, J. et al. Printable two-dimensional superconducting monolayers. *Nat. Mater.* **20**, 181–187 (2021).
64. Hor, Y. S. et al. Superconductivity in Cu₂Bi₂Se₃ and its implications for pairing in the undoped topological insulator. *Phys. Rev. Lett.* **104**, 057001 (2010).
65. Zhang, H. et al. Enhancement of superconductivity in organic-inorganic hybrid topological materials. *Sci. Bull.* **65**, 188–193 (2020).
66. Zhou, B. et al. A chemical-dedoping strategy to tailor electron density in molecular-intercalated bulk monolayer MoS₂. *Nat. Synth.* **3**, 67–75 (2023).
67. Zhu, G. et al. Tuning thermal conductivity in molybdenum disulfide by electrochemical intercalation. *Nat. Commun.* **7**, 13211 (2016).
68. Kang, J. S., Ke, M. & Hu, Y. Ionic intercalation in two-dimensional van der Waals materials: in situ characterization and electrochemical control of the anisotropic thermal conductivity of black phosphorus. *Nano Lett.* **17**, 1431–1438 (2017).
69. Sood, A. et al. An electrochemical thermal transistor. *Nat. Commun.* **9**, 4510 (2018).
70. Wan, C. et al. Flexible n-type thermoelectric materials by organic intercalation of layered transition metal dichalcogenide TiS₂. *Nat. Mater.* **14**, 622–627 (2015).
71. Wan, C. et al. Intercalation: building a natural superlattice for better thermoelectric performance in layered chalcogenides. *J. Electron. Mater.* **40**, 1271–1280 (2011).
72. Soluyanov, A. A. et al. Type-II Weyl semimetals. *Nature* **527**, 495–498 (2015).
73. Jiang, J. et al. Signature of type-II Weyl semimetal phase in MoTe₂. *Nat. Commun.* **8**, 13973 (2017).
74. Peng, J. et al. High phase purity of large-sized 1T'-MoS₂ monolayers with 2D superconductivity. *Adv. Mater.* **31**, 1900568 (2019).
75. Friend, R. H. & Yoffe, A. D. Electronic properties of intercalation complexes of the transition metal dichalcogenides. *Adv. Phys.* **36**, 1–94 (1987).
76. Jung, N. et al. Charge transfer chemical doping of few layer graphenes: charge distribution and band gap formation. *Nano Lett.* **9**, 4133–4137 (2009).
77. Musa, M. R. K. et al. Li interaction-induced phase transition from black to blue phosphorene. *Phys. Rev. Mater.* **5**, 024007 (2021).
78. Zhai, W. et al. Reversible semimetal-semiconductor transition of unconventional-phase WS₂ nanosheets. *J. Am. Chem. Soc.* **145**, 13444–13451 (2023).
79. Tian, B. et al. Phase transformations in TiS₂ during K intercalation. *ACS Energy Lett.* **2**, 1835–1840 (2017).
80. Rasouli, H. R. et al. Electric-field-induced reversible phase transitions in a spontaneously ion-intercalated 2D metal oxide. *Nano Lett.* **21**, 3997–4005 (2021).
81. Yang, R. et al. 2D transition metal dichalcogenides for photocatalysis. *Angew. Chem. Int. Ed.* **62**, e202218016 (2023).
82. Manzel, S., Ovchinnikov, D., Pasquier, D., Yazyev, O. V. & Kis, A. 2D transition metal dichalcogenides. *Nat. Rev. Mater.* **2**, 17033 (2017).
83. Li, W., Qian, X. & Li, J. Phase transitions in 2D materials. *Nat. Rev. Mater.* **6**, 829–846 (2021).
84. Yang, J. J., Strukov, D. B. & Stewart, D. R. Memristive devices for computing. *Nat. Nanotechnol.* **8**, 13–24 (2013).
85. Wang, Y. et al. Li intercalation in an MoSe₂ electrocatalyst: in situ observation and modulation of its precisely controllable phase engineering for a high-performance flexible Li-S battery. *Carbon Energy* **5**, e255 (2023).
86. Wang, M. et al. A gapped phase in semimetallic Td-WTe₂ induced by lithium intercalation. *Adv. Mater.* **34**, 2200861 (2022).
87. Wu, J. et al. Solution processing for lateral transition-metal dichalcogenides homojunction from polymorphic crystal. *J. Am. Chem. Soc.* **141**, 592–598 (2019).
88. Zhu, Z. & Tománek, D. Semiconducting layered blue phosphorus: a computational study. *Phys. Rev. Lett.* **112**, 176802 (2014).
89. Voiry, D. et al. Enhanced catalytic activity in strained chemically exfoliated WS₂ nanosheets for hydrogen evolution. *Nat. Mater.* **12**, 850–855 (2013).
90. Acerce, M., Voiry, D. & Chhowalla, M. Metallic 1T phase MoS₂ nanosheets as supercapacitor electrode materials. *Nat. Nanotechnol.* **10**, 313–318 (2015).
91. Yao, J. et al. Optical transmission enhancement through chemically tuned two-dimensional bismuth chalcogenide nanoplates. *Nat. Commun.* **5**, 5670 (2014).
92. Holzwarth, N. A. W., Louie, S. G. & Rabii, S. Lithium-intercalated graphite: self-consistent electronic structure for stages one, two, and three. *Phys. Rev. B* **28**, 1013–1025 (1983).
93. Bao, W. et al. Approaching the limits of transparency and conductivity in graphitic materials through lithium intercalation. *Nat. Commun.* **5**, 4224 (2014).
94. Xiong, F. et al. Li intercalation in MoS₂: in situ observation of its dynamics and tuning optical and electrical properties. *Nano Lett.* **15**, 6777–6784 (2015).
- A representative work on in situ optical microscope observation of intercalation in 2D materials, examining the Li⁺ intercalation and de-intercalation process in 2D MoS₂, indicating that intercalation of foreign species normally starts from the edge of 2D materials and gradually extends to the whole flake.**
95. Wan, J. et al. In situ investigations of Li-MoS₂ with planar batteries. *Adv. Energy Mater.* **5**, 1401742 (2015).
96. Zhang, R. et al. Breaking the cut-off wavelength limit of GaTe through self-driven oxygen intercalation in air. *Adv. Sci.* **9**, 2103429 (2022).
97. Kanetani, K. et al. Ca intercalated bilayer graphene as a thinnest limit of superconducting C₆Ca. *Proc. Natl Acad. Sci. USA* **109**, 19610–19613 (2012).
98. Yang, S. L. et al. Superconducting graphene sheets in CaC₆ enabled by phonon-mediated interband interactions. *Nat. Commun.* **5**, 3493 (2014).
99. Zhang, R., Waters, J., Geim, A. K. & Grigorieva, I. V. Intercalant-independent transition temperature in superconducting black phosphorus. *Nat. Commun.* **8**, 15036 (2017).
100. Lian, C.-S., Si, C., Wu, J. & Duan, W. First-principles study of Na-intercalated bilayer NbSe₂: suppressed charge-density wave and strain-enhanced superconductivity. *Phys. Rev. B* **96**, 235426 (2017).
101. Morosan, E. et al. Superconductivity in Cu₂TiSe₂. *Nat. Phys.* **2**, 544–550 (2006).
102. Wu, H. et al. Spacing dependent and cation doping independent superconductivity in intercalated 1T 2D SnSe₂. *2D Mater.* **6**, 045048 (2019).
103. Vithanage, D. et al. Electrochemical Li intercalation in b-As₂P_{1-x} alloys: in-situ Raman spectroscopy study. *J. Alloy Compd.* **968**, 171849 (2023).
104. Verzhbitskiy, I. A. et al. Controlling the magnetic anisotropy in Cr₂Ge₂Te₆ by electrostatic gating. *Nat. Electron.* **3**, 460–465 (2020).
105. Huang, X. et al. Li-ion intercalation enhanced ferromagnetism in van der Waals Fe₃GeTe₂ bilayer. *Appl. Phys. Lett.* **119**, 012405 (2021).
106. Mi, M. et al. Variation between antiferromagnetism and ferrimagnetism in NiPS₃ by electron doping. *Adv. Funct. Mater.* **32**, 2112750 (2022).
107. Wang, G., Yu, M. & Feng, X. Carbon materials for ion-intercalation involved rechargeable battery technologies. *Chem. Soc. Rev.* **50**, 2388–2443 (2021).
108. Huang, Z. et al. Anion chemistry in energy storage devices. *Nat. Rev. Chem.* **7**, 616–631 (2023).
109. Yang, R. et al. Fabrication of liquid cell for in situ transmission electron microscopy of electrochemical processes. *Nat. Protoc.* **18**, 555–578 (2023).
110. Zeng, Z. et al. In situ study of lithiation and delithiation of MoS₂ nanosheets using electrochemical liquid cell transmission electron microscopy. *Nano Lett.* **15**, 5214–5220 (2015).
111. Lacey, S. D. et al. Atomic force microscopy studies on molybdenum disulfide flakes as sodium-ion anodes. *Nano Lett.* **15**, 1018–1024 (2015).
112. Wan, J. et al. Ultra-thin solid electrolyte interphase evolution and wrinkling processes in molybdenum disulfide-based lithium-ion batteries. *Nat. Commun.* **10**, 3265 (2019).
113. Hui, J., Burgess, M., Zhang, J. & Rodríguez-López, J. Layer number dependence of Li⁺ intercalation on few-layer graphene and electrochemical imaging of its solid-electrolyte interphase evolution. *ACS Nano* **10**, 4248–4257 (2016).

114. Ji, J.-Y. et al. Homogeneous lateral lithium intercalation into transition metal dichalcogenides via ion backgating. *Nano Lett.* **22**, 7336–7342 (2022).
115. Zielinski, P. et al. Probing exfoliated graphene layers and their lithiation with microfocused X-rays. *Nano Lett.* **19**, 3634–3640 (2019).
116. Zhao, S. Y. F. et al. Controlled electrochemical intercalation of graphene/h-BN van der Waals heterostructures. *Nano Lett.* **18**, 460–466 (2018).
117. Azhagurajan, M., Kajita, T., Itoh, T., Kim, Y.-G. & Itaya, K. In situ visualization of lithium ion intercalation into MoS₂ single crystals using differential optical microscopy with atomic layer resolution. *J. Am. Chem. Soc.* **138**, 3355–3361 (2016).
118. Sun, J. et al. A phosphorene–graphene hybrid material as a high-capacity anode for sodium-ion batteries. *Nat. Nanotechnol.* **10**, 980–985 (2015).
119. Wang, L., Xu, Z., Wang, W. & Bai, X. Atomic mechanism of dynamic electrochemical lithiation processes of MoS₂ nanosheets. *J. Am. Chem. Soc.* **136**, 6693–6697 (2014).
120. Gao, P., Wang, L., Zhang, Y., Huang, Y. & Liu, K. Atomic-scale probing of the dynamics of sodium transport and intercalation-induced phase transformations in MoS₂. *ACS Nano* **9**, 11296–11301 (2015).
121. Hwang, S. et al. Multistep lithiation of tin sulfide: an investigation using in situ electron microscopy. *ACS Nano* **12**, 3638–3645 (2018).
122. Nie, A. et al. Selective ionic transport pathways in phosphorene. *Nano Lett.* **16**, 2240–2247 (2016).
123. Kim, S., Cui, J., Dravid, V. P. & He, K. Orientation-dependent intercalation channels for lithium and sodium in black phosphorus. *Adv. Mater.* **31**, 1904623 (2019).
124. Zhang, L. et al. Electrochemical reaction mechanism of the MoS₂ electrode in a lithium-ion cell revealed by in situ and operando X-ray absorption spectroscopy. *Nano Lett.* **18**, 1466–1475 (2018).
125. Rajapakse, M. et al. Electrochemical Li intercalation in black phosphorus: in situ and ex situ studies. *J. Phys. Chem. C* **124**, 10710–10718 (2020).
126. Hong, X. et al. Ultrafast charge transfer in atomically thin MoS₂/WS₂ heterostructures. *Nat. Nanotechnol.* **9**, 682–686 (2014).
127. Li, F. et al. In situ study of K⁺ electrochemical intercalating into MoS₂ flakes. *J. Phys. Chem. C* **123**, 5067–5072 (2019).
128. Pondick, J. V. et al. The effect of mechanical strain on lithium staging in graphene. *Adv. Electron. Mater.* **7**, 2000981 (2021).
129. Yadegari, H. et al. Operando measurement of layer breathing modes in lithiated graphite. *ACS Energy Lett.* **6**, 1633–1638 (2021).
130. Xue, W. et al. Intercalation-conversion hybrid cathodes enabling Li–S full-cell architectures with jointly superior gravimetric and volumetric energy densities. *Nat. Energy* **4**, 374–382 (2019).
131. Kim, W. J. et al. Geometric frustration of Jahn–Teller order in the infinite-layer lattice. *Nature* **615**, 237–243 (2023).
132. Kuai, L. et al. Revealing crystallization dynamics and the compositional control mechanism of 2D perovskite film growth by in situ synchrotron-based GIXRD. *ACS Energy Lett.* **5**, 8–16 (2020).
133. Li, L. et al. Visualization of electrochemically driven solid-state phase transformations using operando hard X-ray spectro-imaging. *Nat. Commun.* **6**, 6883 (2015).
134. Lim, J. et al. Origin and hysteresis of lithium compositional spatiodynamics within battery primary particles. *Science* **353**, 566–571 (2016).
135. Mefford, J. T. et al. Correlative operando microscopy of oxygen evolution electrocatalysts. *Nature* **593**, 67–73 (2021).
136. Liu, T. et al. Origin of structural degradation in Li-rich layered oxide cathode. *Nature* **606**, 305–312 (2022).
137. Li, J. et al. Dynamics of particle network in composite battery cathodes. *Science* **376**, 517–521 (2022).
138. Man, M. K. L. et al. Imaging the motion of electrons across semiconductor heterojunctions. *Nat. Nanotechnol.* **12**, 36–40 (2017).
139. Lv, B., Qian, T. & Ding, H. Angle-resolved photoemission spectroscopy and its application to topological materials. *Nat. Rev. Phys.* **1**, 609–626 (2019).
140. Zhang, H. et al. Angle-resolved photoemission spectroscopy. *Nat. Rev. Method. Prime.* **2**, 54 (2022).
141. Yang, H. et al. Visualizing electronic structures of quantum materials by angle-resolved photoemission spectroscopy. *Nat. Rev. Mater.* **3**, 341–353 (2018).
142. Reimann, J. et al. Subcycle observation of lightwave-driven Dirac currents in a topological surface band. *Nature* **562**, 396–400 (2018).
143. Karni, O. et al. Structure of the moiré exciton captured by imaging its electron and hole. *Nature* **603**, 247–252 (2022).
144. Park, S. et al. Enhancing catalytic activity of MoS₂ basal plane s-vacancy by co-cluster addition. *ACS Energy Lett.* **3**, 2685–2693 (2018).
145. Kim, H. W. et al. Efficient hydrogen peroxide generation using reduced graphene oxide-based oxygen reduction electrocatalysts. *Nat. Catal.* **1**, 282–290 (2018).
146. Du, L. et al. Moiré photonics and optoelectronics. *Science* **379**, eadg0014 (2023).
147. Zhao, B. et al. High-order superlattices by rolling up van der Waals heterostructures. *Nature* **591**, 385–390 (2021).
148. Cui, X. et al. Rolling up transition metal dichalcogenide nanoscrolls via one drop of ethanol. *Nat. Commun.* **9**, 1301 (2018).
149. Liang, L. et al. Inducing ferromagnetism and Kondo effect in platinum by paramagnetic ionic gating. *Sci. Adv.* **4**, earr2030 (2018).
150. Huang, Y. et al. Hybrid superlattices of two-dimensional materials and organics. *Chem. Soc. Rev.* **49**, 6866–6883 (2020).
151. Wang, A., Li, J. & Zhang, T. Heterogeneous single-atom catalysis. *Nat. Rev. Chem.* **2**, 65–81 (2018).
152. Liu, Y. et al. Van der Waals heterostructures and devices. *Nat. Rev. Mater.* **1**, 16042 (2016).
153. Joensen, P., Frindt, R. F. & Morrison, S. R. Single-layer MoS₂. *Mater. Res. Bull.* **21**, 457–461 (1986).
154. Eda, G. et al. Photoluminescence from chemically exfoliated MoS₂. *Nano Lett.* **11**, 5111–5116 (2011).
155. Zeng, Z. et al. Single-layer semiconducting nanosheets: high-yield preparation and device fabrication. *Angew. Chem. Int. Ed.* **50**, 11093–11097 (2011).
156. Tsai, H.-L., Heising, J., Schindler, J. L., Kannewurf, C. R. & Kanatzidis, M. G. Exfoliated–restacked phase of WS₂. *Chem. Mater.* **9**, 879–882 (1997).
157. Voiry, D. et al. Conducting MoS₂ nanosheets as catalysts for hydrogen evolution reaction. *Nano Lett.* **13**, 6222–6227 (2013).
158. Zheng, J. et al. High yield exfoliation of two-dimensional chalcogenides using sodium naphthalene. *Nat. Commun.* **5**, 2995 (2014).
159. Zeng, Z. et al. An effective method for the fabrication of few-layer-thick inorganic nanosheets. *Angew. Chem. Int. Ed.* **51**, 9052–9056 (2012).
160. Zhang, X. et al. Lithiation-induced amorphization of Pd₃P₂S₈ for highly efficient hydrogen evolution. *Nat. Catal.* **1**, 460–468 (2018).
161. Chen, W. et al. Two-dimensional quantum-sheet films with sub-1.2 nm channels for ultrahigh-rate electrochemical capacitance. *Nat. Nanotechnol.* **17**, 153–158 (2022).
162. Jeon, I., Yoon, B., He, M. & Swager, T. M. Hyperstage graphite: electrochemical synthesis and spontaneous reactive exfoliation. *Adv. Mater.* **30**, 1704538 (2018).
163. Yu, W. et al. Chemically exfoliated VSe₂ monolayers with room-temperature ferromagnetism. *Adv. Mater.* **31**, 1903779 (2019).
164. Yu, W. et al. Domain engineering in ReS₂ by coupling strain during electrochemical exfoliation. *Adv. Funct. Mater.* **30**, 2003057 (2020).
165. Yu, W. et al. High-yield exfoliation of monolayer 1T′-MoTe₂ as saturable absorber for ultrafast photonics. *ACS Nano* **15**, 18448–18457 (2021).
166. Huang, Z. et al. Layer-tunable phosphorene modulated by the cation insertion rate as a sodium-storage anode. *Adv. Mater.* **29**, 1702372 (2017).
167. Li, J. et al. Ultrafast electrochemical expansion of black phosphorus toward high-yield synthesis of few-layer phosphorene. *Chem. Mater.* **30**, 2742–2749 (2018).
168. Yang, S. et al. A delamination strategy for thinly layered defect-free high-mobility black phosphorus flakes. *Angew. Chem. Int. Ed.* **57**, 4677–4681 (2018).
169. Wang, N. et al. Electrochemical delamination of ultralarge few-layer black phosphorus with a hydrogen-free intercalation mechanism. *Adv. Mater.* **33**, 2005815 (2021).
170. Shi, H. et al. Ultrafast electrochemical synthesis of defect-free In₂Se₃ flakes for large-area optoelectronics. *Adv. Mater.* **32**, 1907244 (2020).
171. Lin, Z. et al. High-yield exfoliation of 2D semiconductor monolayers and reassembly of organic/inorganic artificial superlattices. *Chem* **7**, 1887–1902 (2021).
172. Peng, J. et al. Stoichiometric two-dimensional non-van der Waals AgCrS₂ with superionic behaviour at room temperature. *Nat. Chem.* **13**, 1235–1240 (2021).
173. Lee, J. et al. Thin-film image sensors with a pinned photodiode structure. *Nat. Electron.* **6**, 590–598 (2023).
174. Conti, S. et al. Printed transistors made of 2D material-based inks. *Nat. Rev. Mater.* **8**, 651–667 (2023).
175. Yan, Z. et al. Highly stretchable van der Waals thin films for adaptable and breathable electronic membranes. *Science* **375**, 852–859 (2022).
176. Su, C.-Y. et al. High-quality thin graphene films from fast electrochemical exfoliation. *ACS Nano* **5**, 2332–2339 (2011).
177. Zhou, F. et al. Electrochemically scalable production of fluorine-modified graphene for flexible and high-energy ionogel-based microsupercapacitors. *J. Am. Chem. Soc.* **140**, 8198–8205 (2018).
178. Ding, Y. et al. Controlled intercalation and chemical exfoliation of layered metal–organic frameworks using a chemically labile intercalating agent. *J. Am. Chem. Soc.* **139**, 9136–9139 (2017).
179. Jeong, S. et al. Tandem intercalation strategy for single-layer nanosheets as an effective alternative to conventional exfoliation processes. *Nat. Commun.* **6**, 5763 (2015).
180. Watts, M. C. et al. Production of phosphorene nanoribbons. *Nature* **568**, 216–220 (2019).
181. Macdonald, T. J. et al. Phosphorene nanoribbon-augmented optoelectronics for enhanced hole extraction. *J. Am. Chem. Soc.* **143**, 21549–21559 (2021).
182. Abu, U. O. et al. Ultra-narrow phosphorene nanoribbons produced by facile electrochemical process. *Adv. Sci.* **9**, 2203148 (2022).
183. Liu, Z. et al. Unzipping of black phosphorus to form zigzag-phosphorene nanobelts. *Nat. Commun.* **11**, 3917 (2020).
184. Yu, W. et al. Facile production of phosphorene nanoribbons towards application in lithium metal battery. *Adv. Mater.* **33**, 2102083 (2021).
185. Akhtar, M. et al. Recent advances in synthesis, properties, and applications of phosphorene. *npj 2D Mater. Appl.* **1**, 5 (2017).
186. Zhang, H. et al. Tailored Ising superconductivity in intercalated bulk NbSe₂. *Nat. Phys.* **18**, 1425–1430 (2022).
187. Pastor, E. et al. Complementary probes for the electrochemical interface. *Nat. Rev. Chem.* **8**, 159–178 (2024).

Acknowledgements

Z.Z. thanks the General Research Fund (GRF) support from the Research Grants Council of the Hong Kong Special Administrative Region, China [Project No. CityU11308923], the Basic Research Project from Shenzhen Science and Technology Innovation Committee

in Shenzhen, China [No. JCYJ20210324134012034], the Applied Research Grant of City University of Hong Kong (Project No. 9667247) and Chow Sang Sang Group Research Fund of City University of Hong Kong (Project No. 9229123) for funding support. Z.Z. is also thankful for the funding provided by the Seed Collaborative Research Fund Scheme of State Key Laboratory of Marine Pollution, which receives research funding from the Innovation and Technology Commission (ITC) of the Hong Kong SAR Government. Any opinions, findings, conclusions or recommendations expressed in this publication do not reflect the views of the Hong Kong SAR Government or the ITC. Q.L. is thankful for a Natural Sciences and Engineering Research Council of Canada (NSERC) Discovery Grant and an Alberta Innovates Advance Program–NSERC Alliance Grant. J.G. thanks the Advanced Light Source–U.S. DOE Office of Science User Facility under Contract No. DE-AC02-05CH11231.

Author contributions

Z.Z. proposed the topic of the Review. R.Y., L.M., J.L. and Z.Z. co-wrote the manuscript. R.Y., L.M. and Z.L. contributed equally to this work. All authors contributed to the revisions and edits of the manuscript.

Competing interests

The authors declare no competing interests.

Additional information

Supplementary information The online version contains supplementary material available at <https://doi.org/10.1038/s41570-024-00605-2>.

Publisher's note Springer Nature remains neutral with regard to jurisdictional claims in published maps and institutional affiliations.

Springer Nature or its licensor (e.g. a society or other partner) holds exclusive rights to this article under a publishing agreement with the author(s) or other rightsholder(s); author self-archiving of the accepted manuscript version of this article is solely governed by the terms of such publishing agreement and applicable law.

© Springer Nature Limited 2024

¹Department of Materials Science and Engineering and State Key Laboratory of Marine Pollution, City University of Hong Kong, Kowloon, Hong Kong, P. R. China. ²Department of Chemical and Petroleum Engineering, University of Calgary, Calgary, Alberta, Canada. ³Department of Chemistry, Engineering Research Center of Advanced Rare Earth Materials (Ministry of Education), Tsinghua University, Beijing, China. ⁴Department of Chemistry, Seoul National University, Seoul, Republic of Korea. ⁵Advanced Light Source, Energy Storage and Distributed Resources Division, and Material Sciences Division, Lawrence Berkeley National Laboratory, Berkeley, CA, USA. ⁶Walker Department of Mechanical Engineering, The University of Texas at Austin, Austin, TX, USA. ⁷Center for 2D Quantum Heterostructures, Institute for Basic Science, and Department of Energy Science, Sungkyunkwan University (SKKU), Suwon, Republic of Korea. ⁸Institut Européen des Membranes, IEM, UMR, Université Montpellier, ENSCM, CNRS, Montpellier, France. ⁹Department of Nuclear Science and Engineering and Department of Materials Science and Engineering, Massachusetts Institute of Technology, Cambridge, MA, USA. ¹⁰Shenzhen Research Institute, City University of Hong Kong, Shenzhen, China. ¹¹These authors contributed equally: Ruijie Yang, Liang Mei, Zhaoyang Lin.